On the Photochemistry of Methane and Ethane in the Martian Atmosphere: Towards Indirect Detection of Methane Emissions

Benjamin M. Taysum[1,2] **and Paul I. Palmer**[1,2]

[1]School of GeoSciences, University of Edinburgh, Edinburgh, UK
[2]Centre for Exoplanet Science, University of Edinburgh, Edinburgh, UK

Key Points:

- Photochemical products of methane (CH_4) can be used to test indirectly presence of atmospheric CH_4.
- Formaldehyde and formic acid are two key photochemical products of CH_4 and ethane (C_2H_6).
- Oxidation of CH_4 and C_2H_6 produce distinct profiles of photochemical products.
- Photolysis of acetaldehyde, produced by C_2H_6 photochemistry, is a small but significant source of atmospheric CH_4.

Corresponding author: Benjamin M. Taysum, Ben.Taysum@ed.ac.uk

Abstract

Detecting the presence of atmospheric methane (CH_4) on Mars is an ongoing scientific debate, with multiple observations reporting elevated CH_4 amounts that are difficult to reconcile with photochemistry models that describe Martian atmospheric chemistry. We develop an existing 1-D photochemistry model to include a more comprehensive description of organic chemistry, including the oxidation products of CH_4 and ethane (C_2H_6), a longer-chain hydrocarbon that often accompanies abiotic releases of CH_4 on Earth. We report the atmospheric lifetime of CH_4 as a function of altitude along its solar orbit, highlighting regions above the water vapour saturation point where the abundance of $O(^1D)$ reduces the lifetime to 25–60 years, and a region between 50 and 70 km where loss rates are at a minimum that result in a lifetime in excess of 1000 years. We find the two largest photochemical products of CH_4 and C_2H_6 are formaldehyde (HCHO) and formic acid (HCOOH). We show that a 14 ppb uniform profile of CH_4 photochemically results in a latitude-independent layered structure of HCHO at 20–40 km during the Martian northern summer with magnitudes peaking at 0.2 ppt, and oxidation of C_2H_6 produces HCHO at rates an order of magnitude larger than for CH_4. Formic acid is found to have atmospheric lifetimes spanning 10–200 sols below 10 km that show little temporal or zonal variability, and is produced in greater abundances by the oxidation of C_2H_6 than of CH_4. The photochemistry of C_2H_6 has allowed us to identify an atmospheric source of CH_4 from the UV photolysis of acetaldehyde.

Plain Language Summary

Detection of atmospheric CH_4 in the Martian atmosphere remains a scientific challenge to reconcile with photochemical model calculations of atmospheric CH_4, suggesting a missing loss process and/or errors in the available data. Here we use a photochemical model of CH_4 and its oxidation products to explore how high-yield oxidation products of formaldehyde and formic acid that are now observable from orbiting satellites can help reconcile the mismatch between models and data. We also investigate the production of CH_4 from the oxidation of ethane, which often accompanies CH_4 emissions on Earth, and show it represents a small but significant source of atmospheric CH_4 through the UV photolysis of acetaldehyde.

1 Introduction

There is considerable debate in the community about the validity and robustness of detections of atmospheric methane (CH_4) on Mars. Detections and non-detections of atmospheric CH_4 have been reported using data collected by satellites (Formisano et al., 2004; Geminale et al., 2011; Fonti & Marzo, 2010; Geminale et al., 2008; Giuranna et al., 2019), Earth-based telescopes (Mumma et al., 2009; Villanueva et al., 2013; Krasnopolsky, 2012; V. A. Krasnopolsky, 2007; Krasnopolsky, 2011; Krasnopolsky et al., 2004; V. Krasnopolsky et al., 1997) and *in situ* instruments (Webster et al., 2018, 2015; Moores et al., 2019). This debate highlights the difficulty of measuring atmospheric CH_4 on Mars, and the gaps in our current understanding of the production and loss terms that determine atmospheric CH_4 on Mars. We explore how the presence of CH_4 could be determined by its oxidation products and in the process discuss how abiotic CH_4 could be potentially produced by organic chemistry.

Detections of atmospheric CH_4 at the Gale crater by the NASA Curiosity rover were observed episodically rising from mean volume mixing ratios (VMRs) of 0.69 ± 0.25 parts per billion (ppb) to 7.20 ± 2.10 ppb across a 60-sol period (Webster et al., 2015), and the diurnal variations of CH_4 observations via Curiosity have recently been constrained by the ExoMars Trace Gas Orbiter's Nadir and Occultation for Mars Discovery (NOMAD) spectrometer (Moores et al., 2019; Korablev et al., 2019). Ground-based telescopes reported a signal during northern hemisphere midsummer of a plume that contained ap-

proximately 19,000 tonnes of CH_4 (Mumma et al., 2009) near the Syrtis Major region, consistent with an estimated 0.60 kg $m^{-2}s^{-1}$ seasonal point source of organic compounds. Other searches for CH_4 on Mars have conversely failed to detect the compound (Webster et al., 2013), including the Trace Gas Orbiter's year and a half long search(Korablev et al., 2019). This highlights the possibility of methane being significantly more temporally variable than current models predict (Lefèvre & Forget, 2009). This inconsistency with regards to CH_4's detection has also ignited some polemic against the existance of the gas on Mars (Zahnle et al., 2011). Recent analysis of data from the Planetary Fourier Spectrometer (PFS) aboard the Mars Express orbiter identified the presence of CH_4 in the Martian atmosphere that was confirmed via independent observations by Giuranna et al. (2019). These results appear to confirm Curiosity's detection of CH_4 at the Gale Crater. The team retrieved column integrated VMRs of 15.5 $\pm$ 2.50 ppb above the Gale Crater only 1 Martian day (sol) after the Curiosity rover's measurement of a 5.78 $\pm$ 2.27 ppb (Webster et al., 2015).

To further study these possible emissions of CH_4, and to also provide a more detailed series of observations of the vertical structure and composition of Mars' atmosphere, the ExoMars mission program was established by the European Space Agency (ESA) (Vago et al., 2015) and the Russian Roscosmos State Corporation for Space Activities. The first mission conducted within this program was the launch of the Trace Gas Orbiter (TGO) in 2016, that included two suites of spectrometers, the Nadir and Occultation for MArs Discovery (NOMAD) spectrometer (Vandaele et al., 2018) and the Atmospheric Chemistry Suite (ACS) (Korablev et al., 2017). The TGO underwent 11 months of aerobraking to reduce its orbital speed and altitude, eventually establishing an approximately circular orbit of altitude roughly 400 km allowing scientific observations to start in April 2018 (Vandaele et al., 2019). Over the first year, no successful observations of CH_4 were reported by the TGO instrumentation (Korablev et al., 2019). We developed our investigation bearing in mind the capibilities of TGO instruments, especially the solar occultation channels of NOMAD (NOMAD-SO) and ACS (ACS-MIR). The NOMAD-SO instrument has been designed to be sensitive to CH_4 abundances as low as 0.025 ppb when observed in solar occultation mode (Robert et al., 2016). This expected detection limit was confronted to the experimental values in (Vandaele et al., 2019). The TGO instruments improved the experimental upper limit of previous instrumentation to reach a limit of roughly 0.05 ppb for methane. A few profiles reported in Vandaele et al. (2019) and obtained via ACS-MIR, measured in clear northern conditions, were able to achieve the most precise detection limits of 0.012 ppb down to an altitude of roughly 3 km.

Previous studies using 1-D photochemical models (Wong et al., 2003; Summers et al., 2002) calculate the photochemical lifetime of CH_4 to be roughly 300 years below 70 km. In the absence of a strong surface loss process, surface emissions of CH_4 will then become homogeneously distributed across the planet after being introduced into the atmosphere. This inconsistency between models and data means that the available atmospheric data is misinterpreted, and/or there is a loss mechanism that we do no not currently consider in models (V. A. Krasnopolsky, 2006). Previous calculations using a global 3-D general circulation model have determined that to reconcile models and data we need a CH_4 loss process that is up to 600 times faster than any known process (Lefèvre & Forget, 2009). That additional sink would lower the atmospheric lifetime of CH_4 from centuries to less than 200 days. With the advent of the TGO, another approach we can take is to analyse observed spatial and temporal variations of the oxidation products of atmospheric CH_4.

In this study, we describe the development of the 1-D photochemistry submodule from the LMD-UK General Circulation Model (GCM) (Forget et al., 1999; Lewis et al., 1999) to include organic chemistry and run it as an independent model to study photochemistry on Mars. We report results from a series of numerical experiments that describe how the presence of CH_4 affects photochemistry on Mars. We also report photo-

chemical results when we replace CH_4 with ethane (C_2H_6) to show this longer-chain hydrocarbon produced richer atmospheric chemistry but also allows us to consider an abiotic source of atmospheric CH_4 from the oxidation of acetaldehyde. In the next section we describe our developed 1-D model of Mars photochemistry. In section 3 we report results from our numerical experiments. We conclude the paper in section 4 in which we discuss the implications of our results for broadly understanding atmospheric chemistry on Mars but in particular the implications for detecting the presence of CH_4 on Mars from its oxidation products.

2 Methods

3 1-D Photochemical Model

We use the 1-D photochemistry submodule from the parent 3-D LMD-UK Mars General Circulation Model as the basis for a standalone 1-D model that includes an improved treatment of atmospheric organic photochemistry.

We use this standalone 1-D model to describe time-dependent vertical distributions of trace gases from the surface to an altitude of approximately 70 km, described by 25 vertical layers with a resolution of under 0.5km below 2 km increasing to a resolution of 10 km above an altitude of 20 km where 3-D macroscopic processes begin to dominate. We divide a Mars sol into 48 time steps ($\Delta t = 1800$ s), allowing us to describe diurnal variations of trace gases by calculating time-dependent changes in solar zenith angle, taking into consideration changes in solar longitude and axial tilt. To decrease the stiffness of the discretized equations used to compute the photochemical rates of change, determined by a prescribed chemical mechanism described below, we use a chemistry subtimestep of $\Delta t_c = 600$ s.

Vertical tracer transport between model layers is described by classical diffusion equation (Mellor & Yamada, 1982). For details on the vertical diffusion and turbulent mixing routines we refer the reader to Forget et al. (1999). We use a radiative transfer scheme (Madeleine et al., 2011) that uses opacity values from the Mars Climate Database v5.3. We describe the condensation and sublimation of carbon dioxide, (Forget et al., 1998), water ice (Navarro et al., 2014), and hydrogen peroxide (H_2O_2); and an implicit chemistry solver computes production and loss rates from photochemical reactions.

3.1 Organic Photochemistry

The 1-D submodel that resides in the LMD-UK MGCM describes the atmospheric chemistry and transport of 15 trace gases: carbon dioxide (CO_2), carbon monoxide (CO), atomic oxygen (O), singlet oxygen ($O(^1D)$), molecular oxygen (O_2), ozone (O_3), hydrogen atom (H), hydroxy radical (OH), hydroperoxyl radical (HO_2), molecular hydrogen (H_2), hydrogen peroxide (H_2O_2), nitrogen (N_2), argon (Ar), and H_2O as ice and vapour. The photochemistry scheme for these compounds consists of 32 chemical reactions (B1), and 10 photolysis reactions (B2).

We build on the chemical mechanism by including 42 new organic compounds, guided by previous studies (Wong et al., 2003; Summers et al., 2002) and also the theoretical measurement capabilities of the NOMAD instrument (Robert et al., 2016), to improve understanding of Mars' atmospheric chemistry. We include CH_4, C_2H_6 and its photochemical products. The extended chemical mechanism represents an additional 106 chemical reactions (B1) and 29 photolysis reactions (B6). A complete list of trace gas species within the 1-D model is provided in 1.

We take the organic chemistry rate coefficients from the CAABA/MECCA v4.0 atmospheric box model (R. Sander et al., 2019), which is used to model organic chemistry within Earth's atmosphere. We have modified the mechanism to include HCO and

Table 1. Trace gas species handled by the 1-D photochemistry submodule.

Formula	Name
Inorganic Tracers	
CO_2	Carbon Dioxide
CO	Carbon Monoxide
$O(^1D)$	Atomic Oxygen (excited singlet)
$O \equiv O(^3P)$	Atomic Oxygen (ground-state)
O_2	Molecular Oxygen
O_3	Ozone
H	Atomic Hydrogen
OH	Hydroxyl
HO_2	Hydroperoxyl
H_2O_2	Hydrogen Peroxide
H_2	Molecular Hydrogen
H_2O (vapour and ice)	Water Vapour and Ice
N_2	Nitrogen
Ar	Argon
Organic Tracers (Methane Oxidation)	
CH_4	Methane
CH_3	Methyl Radical
CH_3O_2	Methyl Peroxy-radical
CH_3OOH	Methyl Hydroperoxide
CH_3OH	Methanol
CH_3O	Methoxide
HCHO	Formaldehyde
HCOOH	Formic Acid
$HOCH_2O_2$	Hydromethyl Peroxy
$HOCH_2OH$	Methanediol
$HOCH_2OOH$	Hydromethyl Hydroperoxide
HCO	Formyl Radical
Organic Tracers (Ethane Oxidation)	
C_2H_6	Ethane
C_2H_5	Ethyl Radical
$C_2H_5O_2$	Ethyldioxy Radical
C_2H_5OOH	Ethyl Peroxide
C_2H_5OH	Ethanol
$HOCH_2CH_2O_2$	-
$HOCH_2CH_2O$	-
Ethgly ($(CH_2OH)_2$)	Ethylene Glycol
Hyetho2h ($C_2H_6O_3$)	-
CH_3CHO	Acetaldehyde
CH_2CHOH	Ethenol
CH_3CHOHO_2	Hydroxy Ethyl Peroxy Radical
CH_3COOH	Acetic Acid
$CH_3CHOHOOH$	-
$CH_3C(O)$	Acetyl Radical
$CH_3C(O)OO$	-
$CH_3C(O)OOH$	Peracetic Acid
$HCOCH_2O_2$	-
Glyox (OCHCHO)	Glyoxal
HCOCO	-
$HOOCH_2CHO$	Hydroperoxy Acetaldehyde
$HOCH_2CHO$	Glycolaldehyde
HOCHCHO	Hydroxyl-Vinoxy Radical
$HOCH_2CO$	-
$HOCH_2CO_3$	-
$HOCH_2CO_2H$	Glycolic Acid
$HCOCO_2H$	-
$HCOCO_3H$	-
$HCOCO_3$	-
$HOCH_2CO_3H$	-

C_2H_5 radicals. The CAABA/MECCA v4.0 model neglects these radicals as products, and instead includes the products of the radicals with molecular oxygen, O_2. This approximation is sufficient for Earth, where O_2 is present at 21% mass fraction, but on Mars it is present only at a mass fraction of 10^{-3}. Including these radicals allows us to improve the description of organic chemistry. All three-body reaction rate coefficients in the submodule are multiplied by a factor of 2.5, following Nair et al. (1994), to account for the increase in efficiency that CO_2 displays when used as a bath gas in comparison to N_2 or dry air (Kaufman & Kelso, 1967), commonly used in laboratories for the calculation of these coefficients.

To improve the computational expediency of our chemistry calculation we use a pre-calculated look-up table to interpolate photolytic frequencies. We calculated these photolysis loss rates using the Tropospheric Ultraviolet and Visible (TUV) Radiation Model (Madronich et al., 2002) that has been adapted for use on Mars (Lefèvre et al., 2004), and using routines to interpolate as function of atmospheric temperature, solar zenith angle, O_3 column density, the total atmospheric column density, the Sun-Mars distance, and the dust opacity. The photolytic reaction j_{HOCH_2OOH} of B6 requires the consideration of the abundance of O_2, as the photolytic product of $HOCH_2OOH$ is the highly reactive $HOCH_2O$ radical. $HOCH_2O$ proceeds to react with molecular oxygen to form HCOOH and OH. To limit the number of compounds that the steady-state approximation has to be applied to, the 1-D model multiplies the photolytic frequency extracted from the TUV look-up table by a temperature independent factor of 3.50×10^{-14} (Veyret et al., 1982) and the number density of O_2 at the respective layer.

To improve the accuracy of the original chemistry routine, we decreased the chemical timestep to 100 seconds to decrease the numerical stiffness of the chemistry calculations. This has the additional benefit of allowing the Semi-Implicit Backward Euler Method (SIBEM) to be used for a larger number of species across timestep Δt_c while conserving mass of the studied tracers. For species with photochemical lifetimes shorter than 100 seconds we consider a family of species, e.g. odd-hydrogen (HO_x) and odd-oxygen (O_x) families, which have a collective lifetime longer than the timestep. We handle these compounds, H, OH, HO_2 and $O(^1D)$, $O(^3P)$, O_3 respectively via the assumption of photochemical equilibrium (Rodrigo et al., 1990). The routine calculates dimensionless partition functions of H/HO_2, OH/HO_2, and $O(^3P)/O_3$, and sums the abundances of each family, HO_x and O_x, which possess atmospheric lifetimes greater than that of the chemistry timestep, allowing them to be computed via the SIBEM equation. The partition functions are then applied to compute each individual compounds respective abundance.

3.2 Time-dependent meteorological boundary conditions

To drive the 1-D photochemistry model, we use time-dependent lateral atmospheric boundary conditions of temperature, wind, water vapour volume mixing ratios, and surface pressure from the Mars Climate Database v5.3 (MCD) (Millour et al., 2017). We interpolate the 3-D meteorological fields from the MCD dataset, taking into account latitude, solar longitude, and local time.

All interpolated values from the MCD dataset are longitudinal means, calculated independently by ourselves, acknowledging that there are only small longitudinal variations of meteorological parameters that are due primarily to topographical features. We take advantage of this so that the horizonal footprint of our model is representative of a zonal band of 3.75° in latitude, which is the latitudinal resolution of the MCD dataset. Zonal and meridional transport is not accounted for by the 1-D model. We use an interpolation routine for trace gases that have atmospheric chemistry lifetimes greater than the e-folding residence times associated with meridional advection of trace gases out of the zonal band, which is approximately 0.5–2 sols. We use this approach to drive the model with vertical profiles of CO_2, CO, O_2, H_2, and water vapour, ensuring the photochem-

ical environment is consistent with the meteorological fields from the MCD, allowing the 1-D model to be accurately representative of the temporally and spatially variable oxidising environment. Seasonal water vapour profiles from MCD are especially important for the 1-D photochemical calculations as the photolysis of Martian H_2O is the source of the highly reactive odd-hydrogen species, $HO_x = H + OH + HO_2$, which help drive the oxidation of organic species and O_3 chemistry (Lefèvre et al., 2004).

The overarching purpose of using these boundary conditions is that we can describe detailed 1-D atmospheric chemistry, including diurnal and seasonal changes associated with Mars' atmosphere, without the computational overhead of solving the 3-D dynamical equations. In particular, the boundary conditions help to maintain realistic values and variations of wind profiles that underpin vertical diffusion calculations that correspond to calculating vertical transport. For all of our calculations, we use a prescribed dust scenario produced from the assimilation of observations of the dust optical depth made by the Mars Global Surveyor's Thermal Emission Spectrometer (Montabone et al., 2015) during Mars Year (MY) 24. This scenario is regarded as a 'best guess' of the mean annual dust variability experienced on Mars without the presence of global or significant regional dust storms.

We limit our calculations to latitudes less than 30°, where most recent observations of CH_4 on Mars have been reported (Mumma et al., 2009; Webster et al., 2018, 2015). At latitudes higher than 40° in both hemispheres, the MCD boundary conditions also allow us to describe the large-scale seasonal changes in atmospheric temperature that result from condensation, deposition and sublimation of CO_2, which produce significant changes in surface pressure. However, at these latitudes meridional wind profiles above the planetary boundary layer can become large enough to lower the tracer e-folding timescales to values too small for the 1-D model to neglect while still producing reliable model results. At latitudes less than 30°, the 1-D model in this work can be used to produce time-dependent tracer profiles for periods limited to 2 sols.

3.3 Definition of Numerical Experiments

We use the 1-D model to determine vertical profiles of organic compounds that evolve from a hypothetically fixed and vertically uniform 14 ppb profile of CH_4. We have chosen this value because it was the 3σ upper limit determined by V. A. Krasnopolsky (2007) as part of their analysis of measurements of Mars collected at the NASA Infrared Telescope Facility on Mauna Kea, Hawaii.

For this calculation, we initialise the model 10 sols prior to the point where solar longitude $L_S = 0°$ with initial meteorological conditions and tracer profiles of CO_2, CO, O_2, water vapour, and H_2 from the previously detailed MCD v5.3 look-up table, and 10 ppbv of CH_4 distributed evenly across all 25 atmospheric layers ranging from the surface to approximately 70 km. We then run the 1-D over one Mars year, 668 sols, following a 10 sol spin-up period, taking into account diurnal and seasonal (orbital) variations in solar zenith angle and corresponding changes in solar flux and photolytic frequencies. We report calculations at latitudes of 30°N, 2.5°N, and 30°S to investigate possible spatial variations in organic product profiles.

Following this investigation into the annual variations of the products produced by the steady and homogeneous CH_4 background, we use the 1-D model to investigate time-dependent photochemical processes that result from oxidation of CH_4. For these experiments, we initialise the 1-D model at the required latitude and solar longitude at 00:00 local time (LT) with 0 ppb CH_4 and other non-methane organic compounds. We use a five-day spin-up period at a constant solar longitude when we use trace gas profiles of CO_2, CO, O_2, H_2, and water vapour from the MCD v5.3 (section 3.2) and diurnally-varying atmospheric parameters. This spin-up enables the HO_x and O_x chemistry to partition to the solar-longitude environment. After five sols, we add a vertically-uniform 14 ppb

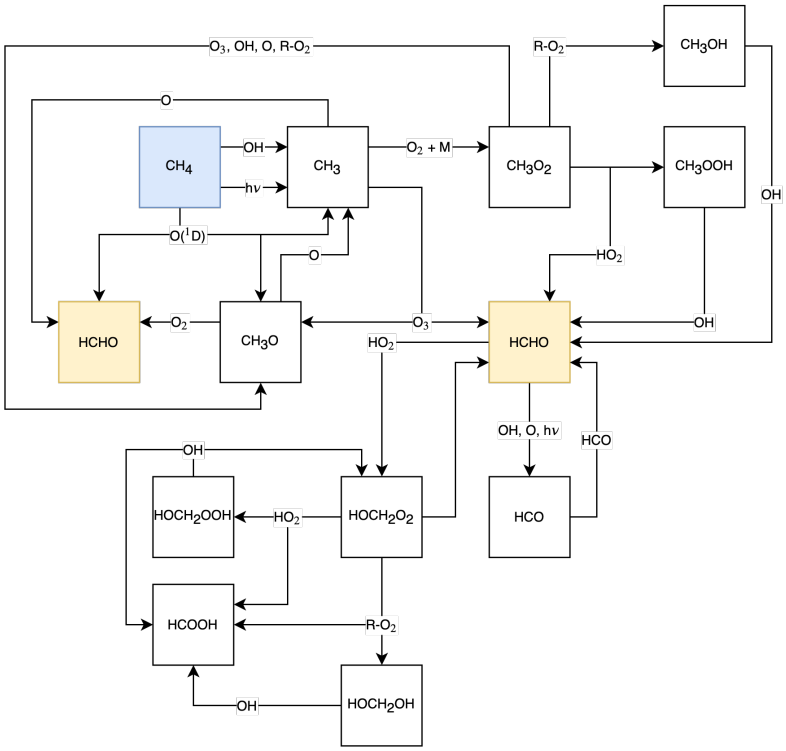

Figure 1. Primary stages of the CH_4 photochemistry that we use in our 1-D photochemistry model, taken from the CAABA/MECCA v4.0 chemical mechanism.

of CH_4 at 00:00 LT. We then let the model run freely for a further two sols, and present the photochemical products from the second day. We adopt a similar approach to examine the photochemistry of C_2H_6.

4 Results

We use the 1-D model described in the previous section to understand the seasonal chemical composition of the Martian atmosphere as a function of latitude that corresponds to a fixed, uniform vertical distribution of atmospheric CH_4. We present a similar set of calculations that correspond to a uniform vertical distribution of atmospheric C_2H_6.

4.1 Methane Oxidation in the Atmosphere of Mars

Figure 1 describes the initial photochemical oxidation steps of atmospheric CH_4 on Mars. The dominant atmospheric losses of CH_4 are oxidation by the hydroxyl radical (OH) and the excited singlet oxygen ($O(^1D)$), and photolysis. The loss rates for atmospheric CH_4 vary as a function of solar longitude. There are a number of high-yield oxidation products that are produced rapidly, potentially allowing us to colocate elevated values with CH_4 emissions, and that are observable from orbiting instruments. In this paper we will restrict our analysis to the production of formaldehyde (HCHO) and formic acid (HCOOH).

Figure 2 shows an illustrative vertical distribution of CH_4 loss factors (s^{-1}) at the solar longitude of 148°, representive of early summer on Mars. Loss factors, units of s^{-1}, are distinguished from loss rates, units of molec. cm^{-3} s^{-1}, as loss factors provide a better insight into the reactivity of the surrounding environment. These values when mul-

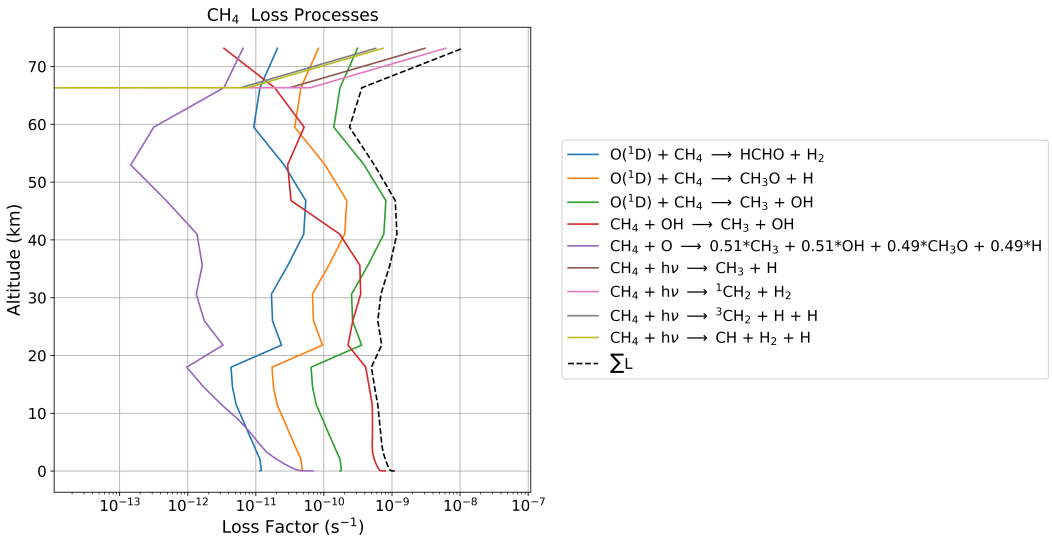

Figure 2. Photochemical loss factors (s^{-1}) CH_4 in our 1-D photochemistry model at latitude 2.5°N, local time 12:00, and solar longitude 148° as a function of altitude.

tiplied by CH_4 number densities equate to the rate of photochemical loss of CH_4, in molec. $cm^{-3}s^{-1}$, i.e. the loss rate. From the surface to roughly 20 km the dominant loss process for CH_4 is from oxidation by OH. At this solar longitude, the hygropause, describing the atmospheric minimum in water vapour is at approximately 20 km at low latitudes in the northern hemisphere. Consequently, at this location OH production rates, driven by the photolysis of water vapour, are larger below 20 km. Above 20 km, the abundance of $O(^1D)$ increases, reflecting the drop in its loss from reaction with water vapour. In the middle atmosphere, between 20 and 60 km, $O(^1D)$ becomes the dominant loss of atmospheric CH_4. There are three oxidation channels associated with this reaction (B4), but the most efficient produce CH_3 and OH. Photolysis of CH_4 becomes significant only at altitudes higher than 60 km. The decreasing abundance of $O(^1D)$ atoms in the upper atmosphere results in a small vertical region, 50–60 km, where CH_4 loss rates decline before photolysis becomes important at higher altitudes.

The net atmospheric lifetime of CH_4, incorporating all loss terms (Figure 2), varies as a function of latitude and solar longitude. Differences between latitudes are determined by the solar radiation being received, which is a function of solar longitude and Mars' obliquity. Atmospheric lifetimes range from 25 to 1700 years (Appendix A1). These values, with a significant and localized surface loss process, would generate a large, slowly varying background value for CH_4 that would be difficult to attribute to individual surface sources. Atmospheric lifetimes reach a minimum of 25–200 years between the top of the hygropause and approximately 50 km due to the larger abundance of the $O(^1D)$ atom. Below the hygropause where OH is the dominant sink, atmospheric lifetimes vary between 200 and 425 years. The longest lifetimes of 1000–1700 years lie between 50 and 60 km during winter (L_S = 270–360°), as described above, where the OH and $O(^1D)$ loss processes decline and before photolysis dominates above 60 km.

Figure 3 shows vertical profiles of the number densities (cm^{-3}) of major organic compounds that result from the oxidation of a fixed, uniformly distribution 14 ppb of atmospheric CH_4. For this calculation we initialised the 1-D model with 0 ppb of CH_4 across all vertical layers at L_S = 148°, 00:00 LT, at a latitude of 2.5°, where a CH_4 plume has been previous observed (Mumma et al., 2009). We spun-up for five sols using detailed MCD v5.3 tracer profiles (section 2). We then inserted a fixed, uniform profile of 14 ppb

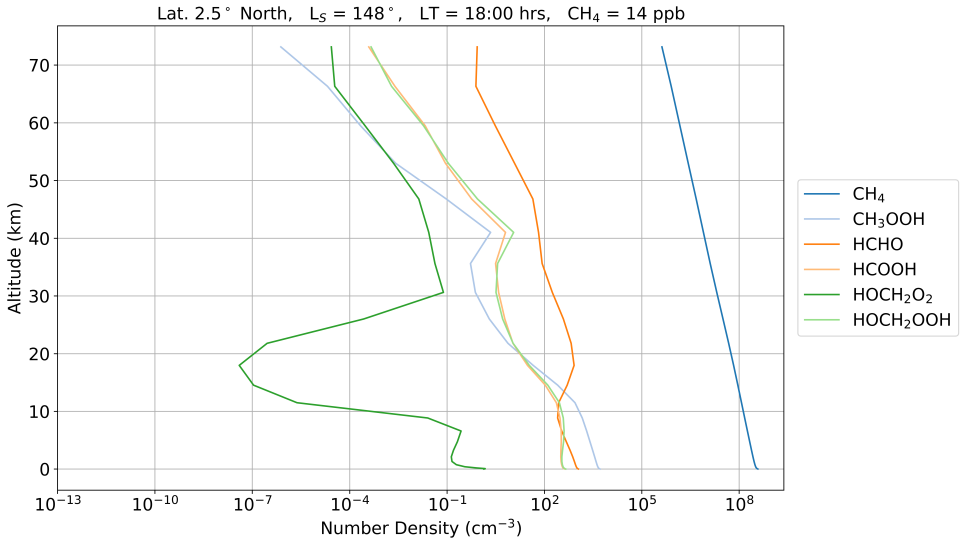

Figure 3. Number density profiles (cm^{-3}) of major photochemical products of 14 ppb of CH_4 after one sol. These include formaldehyde (HCHO), formic acid (HCOOH), methyl hydroperoxide (CH_3OOH), hydromethyl peroxy ($HOCH_2O_2$), and hydromethyl hydroperoxide ($HOCH_2OOH$).

of CH_4 into the model and ran forward for one sol. We sample the model at 18:00 LT on sol 6, allowing sufficient time for products to be produced but a short enough time to ensure these products are not advected out of the column. This allows us to study the resulting CH_4 oxidation product concentrations. We show values for CH_4, HCHO, HCOOH, methyl hydroperoxide (CH_3OOH), hydromethyl peroxy ($HOCH_2O_2$), and hydromethyl hydroperoxide ($HOCH_2OOH$). The two products with the highest photochemical yields are HCHO and HCOOH. We find that HCHO has a column density 1.84×10^9 cm^{-2} and HCOOH has a column density of 5.08×10^8 cm^{-2}. We describe below the responsible production and loss rates associated with these two compounds.

Production of Formaldehyde from CH_4 Oxidation

HCHO is a high-yield oxidation product of CH_4 that is observable by the NOMAD spectrometer aboard the ExoMars Trace Gas Orbiter. Figure 4 shows vertical distributions of HCHO concentrations, corresponding to a fixed vertical profile of 14 ppb CH_4, at 18:00 LT over all solar longitudes to determine when we might expect HCHO to be observable during one Martian year. HCHO production peaks during spring months when there is sufficient production of $O(^1D)$ in the middle atmosphere to oxidize CH_4 but not water vapour in the lower atmosphere. We find only small variations in the HCHO produced across the three latitudes, where HCHO consistently remains below 0.2 ppt. This lies below the expected detection limit of 30–40 ppt for the ExoMars TGO's NOMAD spectrometer (Robert et al., 2016).

Figure 5 shows individual and net production and loss rates of HCHO as a function of altitude at 06:00 LT, $L_S = 93°$ and latitude 2.5°N. The solar longitude of 93° has been chosen due to it coinciding with the temporal region where the layered structure of HCHO's lifetime exists. The 1-D model finds net production to maximise at 06:00 hrs as the sun begins to rise above the horizon. Figure 5a shows two distinct regions where HCHO production peaks. Below the hygropause, at roughly 15 km at this L_S, reaction

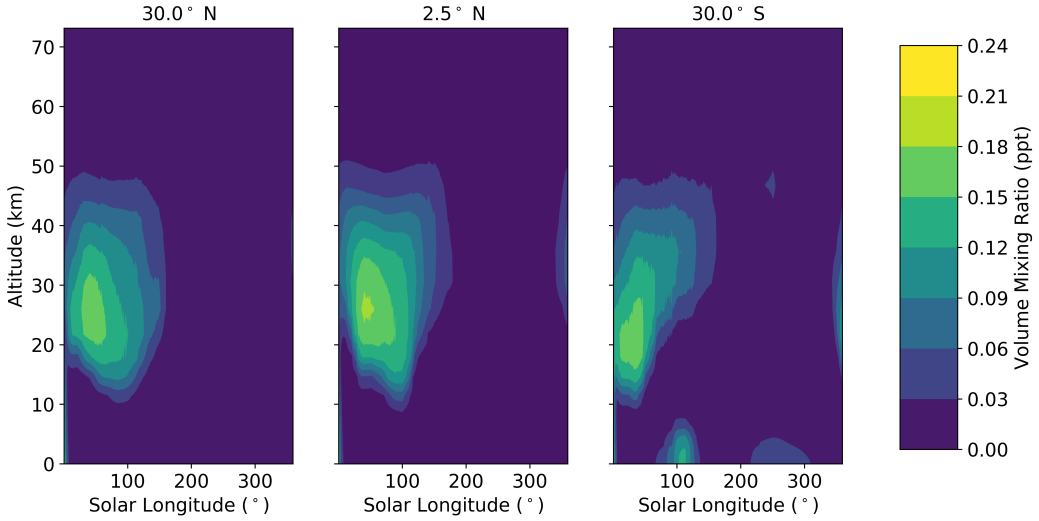

Figure 4. Vertical profiles of HCHO (ppt) from the photochemistry of 14 ppb CH_4 within a zonal band centered on latitudes 30°N, 2.5°N, and 30°S, across all solar longitudes, as calculated by our 1-D photochemical model.

between water vapour and excited atomic oxygen result in HCHO production dominated by the reaction of CH_3O_2 and HO_2. Above the hygropause at 15 km, the HCHO production is from atomic oxygen reacting with methyl and methoxy radicals. Figure 5b show the HCHO loss rates. We find that HCHO is lost rapidly by photolysis through the atmospheric column. Below the hygropause, HCHO is lost by reaction with HO_2 which produced the $HOCH_2O_2$ peroxy radical. Above the hygropause, the dominant HCHO sink is reaction with atomic oxygen. At solar zenith angles between 60 and 85°, abundances of $O(^3P)$, CH_3, and CH_3O radicals are in large enough at the top of the hygropause to overcome the loss of HCHO from photolysis. At lower solar zenith angles, the rate of formaledhyde photolysis is too great to allow significant net production.

The resulting atmospheric lifetime of HCHO for all Martian seasons is 2–6 hours at latitudes less than 30° (Appendix A2), consistent with previously published results (Wong et al., 2003). As a result, a detection of HCHO below 70 km in the Martian atmosphere will require a strong active release of CH_4 in the local vicinity. Our calculations suggest that HCHO will be most likely detected at mid-altitudes (15–30 km) across the tropics during Mars northern spring and summer months. This is due to the lower abundance of water vapor and the increased levels of odd-oxygen species available for reactions with organic radicals, and also coincides with the altitude regions where the TGO instruments are expected to display the greatest level of sensitivity (Korablev et al., 2017).

Production of Formic Acid from CH_4 Oxidation

The oxidation of HCHO via HO_2 radicals leads to pathways that produce HCOOH (Figure 1). HCHO reacts with HO_2 to produce the $HOCH_2O_2$ peroxy radical, which can either decay into its original reactants, or react with HO_2 to produce HCOOH directly or to produce the methoxy radical $HOCH_2OOH$ that subsequently reacts with OH to produce formic acid or $HOCH_2O_2$, with a branching ratio, $k_{HOCH_2O_2}/k_{HCOOH}$, of 0.233 at 298 K. $HOCH_2OOH$ can also photolyse under UV radiation to produce $HOCH_2O$ and

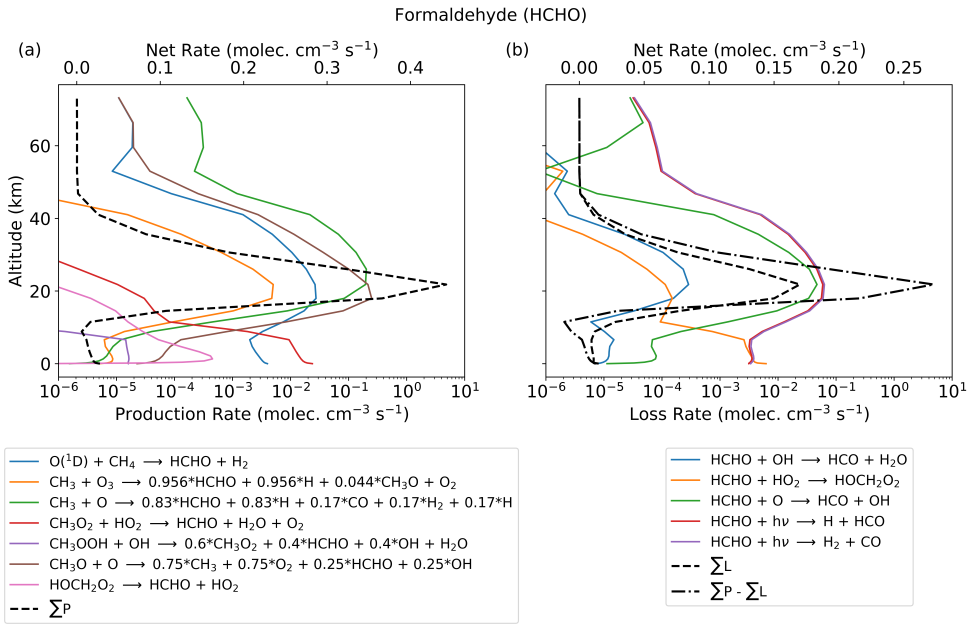

Figure 5. Photochemical production and loss rates for HCHO (molec cm^{-3}s^{-1}), associated with CH_4 photochemistry, as a function of altitude. Calculations are for L_S = 93°, 06:00 LT, and latitude 2.5°N.

OH. The $HOCH_2O$ radical proceeds to react with molecular oxygen to produce formic acid and HO_2. The only sink of HCOOH in the Martian atmosphere is via oxidation by OH. This reaction is slow, and limits loss of HCOOH to regions below the point of the hygropause. In regions where OH concentrations are at a maximum, typically during L_S = 150–340° at the top of the water vapour saturation point, HCOOH has a photochemical lifetime that range between 1 and 10 sols. From the surface to roughly 8 km, values range between 70 sols and 220 sols throughout the year in the northern hemisphere, but values in the south increase to magnitudes of 10^3 sols during the northern summer (L_S = 90–180° with the lower abundances of atmospheric H_2O.

Figure 6 shows the net and individual production and loss rates for HCOOH for L_S = 93°, latitude 2.5°N, and LT = 12:00 hrs due to a fixed, uniformly distribution of 14 ppb CH_4. The largest production rate of HCOOH is from $HOCH_2O_2$ reacting with HO_2 and from the photolysis of $HOCH_2OOH$. The loss of HCOOH from OH oxidation is slow compared to the production rates. Our calculations therefore suggest that a detection of HCOOH would be related to the photochemical loss of HCHO. The resulting atmospheric lifetime of HCOOH is temporally and spatially variant, with lows of 2–5 sols at the tip of the hygropause, increasing to 75–100 sols closer to the surface where the abundances of OH fall.

4.2 Ethane Oxidation

Here we consider the impact of C_2H_6 on Mars' photochemistry. The impetus for these calculations is that on Earth, emissions of CH_4 are accompanied by emissions of higher-chain hydrocarbon such as C_2H_6 (Horita & Berndt, 1999; Guenther et al., 2000). C_2H_6 is also listed as an observable compound through the NOMAD-SO instrument, with detection limits between 0.02 and 0.03 ppb (Vandaele et al., 2018).

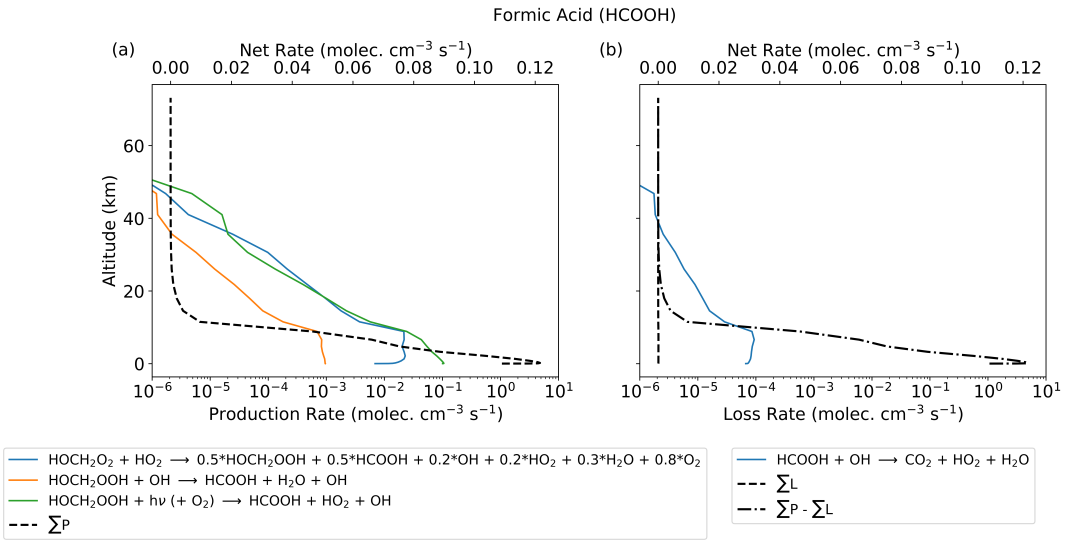

Figure 6. As Figure 5 but for formic acid (HCOOH).

Figure 7 shows that the photochemistry for C_2H_6 is more complicated than for CH_4 (B4), but follows the same general routes. It is oxidized by OH and O(^{1}D) that initiates a series of chemical reactions that result in high yield products of HCHO and HCOOH among other compounds. One of the initial C_2H_6 oxidation product is the C_2H_5 radical, which is not described explicitly by the CAABA mechanism. We have used independent sources for reaction rates that involve the C_2H_5 radical (B5).

Figure 8 shows the photochemical loss factors for C_2H_6 in the Martian atmosphere at noon, L_S 148°, and at latitude 2.5°N. Our photolysis calculations, based on values from the TUV model (Madronich et al., 2002) and adjusted for the Sun–Mars distance, suggest this loss process is insignificant below 70 km. As such we have considered products of C_2H_6 photolysis. Below the hygropause OH is the dominant loss process for C_2H_6 and above the hygropause O is the dominant loss process for C_2H_6, with the $C_2H_5O_2$ peroxy radical being a common oxidation product that results in a cascade of photochemical reactions, as described in Figure 7. The resulting photochemical lifetime of C_2H_6 is typically between 1 and 3.5 years below altitudes of 5 km and much shorter (50–450 sols) above the hygropause. (Appendix A).

Figure 9 shows the vertical profiles of organic compounds produced by the oxidation of 14 ppb of C_2H_6 after one sol at L_S 148°, latitude 2.5° sampled at 18:00 LT, to allow comparisons against the methane investigation of Figure 3. The introduction of longer chain peroxy-radicals via the $C_2H_5O_2$ radical increases the richness of photochemical products that are produced from CH_4 oxidation. In particular, the oxidation of C_2H_6 results in significant column density (3×10^{10} cm^{-2}) of acetaldehyde (CH_3CHO) by 18:00 LT. Photolysis of (CH_3CHO) is a source of CH_4 and carbon monoxide. We find that 14 ppb of C_2H_6 produces a CH_4 column abundance of 1.98×10^{8}cm^{-2} as a result of this photolytic reaction.

Formaldehyde is produced with a higher yield for C_2H_6 oxidation than for CH_4 oxidation, resulting in a column density of 3.01×10^{9} cm^{-2}. We also calculate higher production rates of HCOOH, yielding column abundance of 2.40×10^{10}cm^{-2}. These enhanced yields of HCHO and HCOOH are due to the large number of pathways compared to the CH_4 oxidation mechanism.

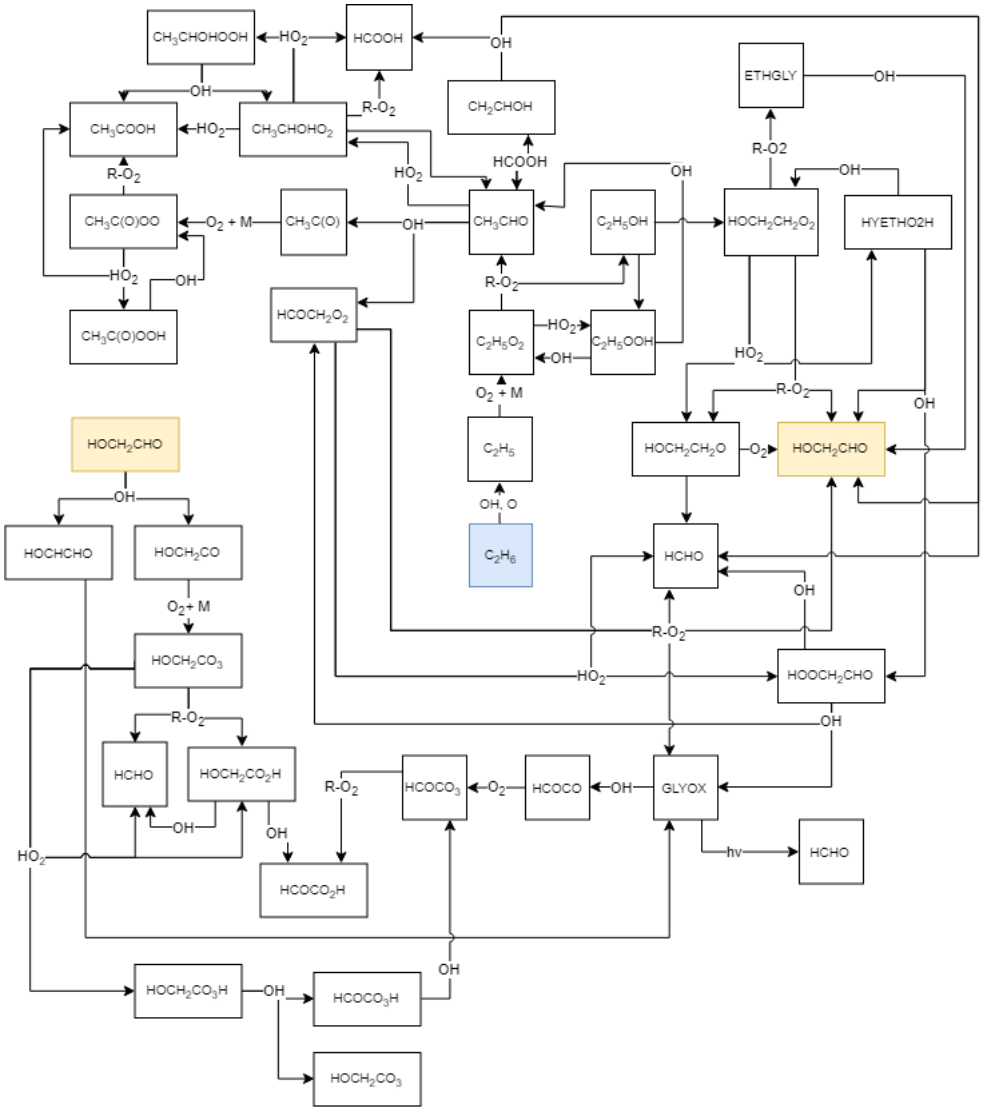

Figure 7. Primary stages of the C_2H_6 photochemistry that we use in out 1-D photochemistry submodule, taken from the CAABA/MECCA v4.0 box model.

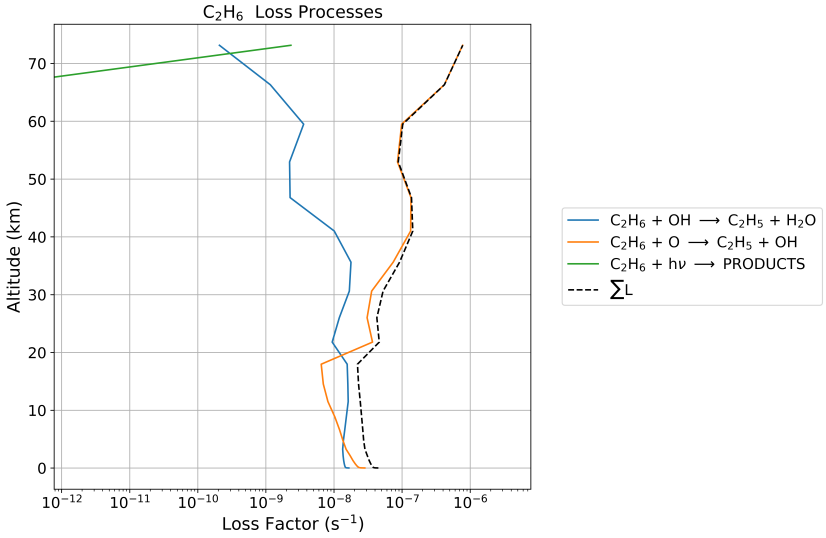

Figure 8. Photochemical loss factors for C_2H_6 as a function of altitude in our 1-D photochemistry model with altitude. Calculations are for $L_S = 148°$, 12:00 LT, and latitude 2.5°N.

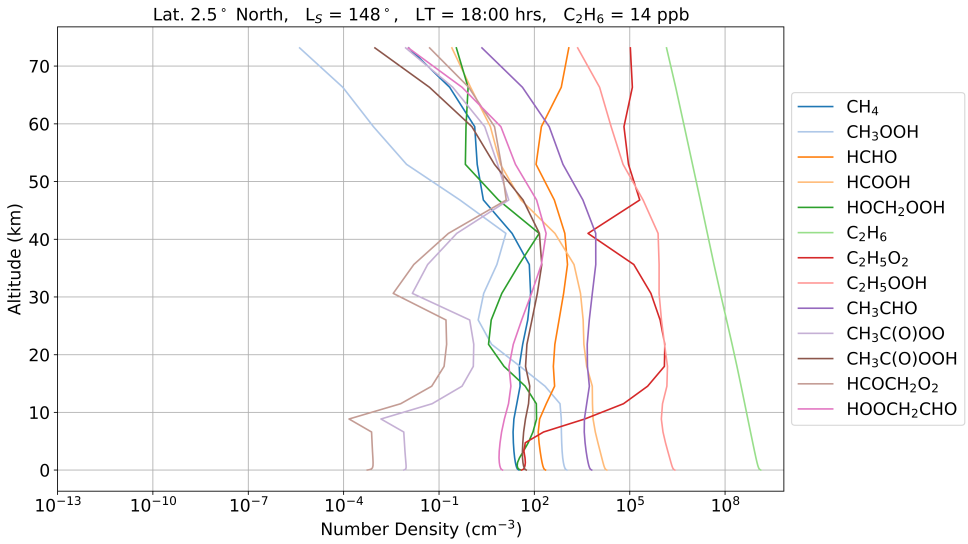

Figure 9. Number density profiles (cm^{-3}) of oxidised organic products after one sol of introducing a uniform profile volume mixing ratio of C_2H_6.

Production of Formaldehyde and Formic Acid from C_2H_6 Oxidation

Figure 10 shows the production and loss rates for HCHO and HCOOH from the oxidation of 14 ppb of C_2H_6. The largest production rate of HCHO is below the hygropause from the reaction of CH_3O_2 peroxy radical with HO_2, comparable to values from CH_4 oxidation. However, above the hygropause at 20 km the three-body reaction $CH_3C(O)+O_2+M$ and the CH_3 radical reaction with atomic oxygen are the primary sources of HCHO. Combined, the HCHO production rate is an order of magnitude larger than the rate from CH_4 oxidation.

The higher reactivity of C_2H_6 produces a larger quantity of $HOCH_2O_2$ peroxy radicals and hydroperoxy radicals in the regions just above the hygropause compared to CH_4 oxidation. With no additional loss processes, the increased net production rate results in larger concentrations of HCOOH, with production falling off rapidly towards the surface.

Methane Production from the Oxidation of Acetaldehyde

Figure 11 shows the number density of acetaldehyde (Figure 9) and the production rate of CH_4 from the photolysis of acetaldehyde. We calculate the photolysis rates using the TUV model (section 2) that penetrate efficiently to the surface. This photolytic source is the only proposed source of CH_4 that may be possible within the CO_2-dominated atmosphere of Mars.

We find that the acetaldehyde produced from the oxidation of the 14 ppb vertically homogeneous C_2H_6 column favours altitudes that are at the top of the hygropause, i.e. altitudes between 15 and 35 km. With the higher abundance of CH_3CHO here, this region is where CH_4 production via atmospheric acetaldehyde will be most effective. From Figure 11, it can be seen that production rates in this altitude band range between 0.01 and 0.20 molecules s^{-1} cm^{-3} while in the presence of ppt magnitudes of CH_3CHO.

5 Discussion and Concluding Remarks

We find that the oxidation of atmospheric CH_4 in the Martian atmosphere, at magnitudes similar to reported observations, produce formaldehyde and formic acid as photochemical products but at concentrations too low for successful detection via remote sensing by the ExoMars TGO's NOMAD spectrometer. Our photochemical lifetimes of formaldehyde are consistent with previous studies (e.g., Wong and Atreya (2004)), but we have also reported variations as a function of altitude and solar longitude. Our use of the MCD v5.3 atmospheric parameters and tracer profiles enabled us to deduce that the largest atmospheric lifetimes of HCHO at latitudes less than 30° are typically around 4 hours during the northern spring and summer above the point of H_2O vapour saturation. Our model expands upon the findings from the steady state model by revealing the layered seasonal structure of HCHO that can develop, whilst refining the modelled lifetimes and revealing the seasonal variability of the compound.

Our 1-D model refines the vertical structure and seasonal variability of the CH_4 within the equatorial regions of Mars, revealing that altitudes with low water vapour content can provide $O(^1D)$ abundances large enough to suppress the lifetime of CH_4 to between 50–100 years, shorter than previous estimates (Wong & Atreya, 2004; Summers et al., 2002; Krasnopolsky et al., 2004). We reveal a region in the upper section of the 1-D model, corresponding to 50–70 km where the absence of OH, $O(^1D)$, and lower UV photolysis increases CH_4 lifetimes to 400–800 years during the northern spring, and to 800–1300 years during the mid-northern summer to northern winter, significantly higher than previous model estimations. Lifetimes close to the surface and below the hygropause (0–30 km) are invariant with latitude during the northern spring, but display variations

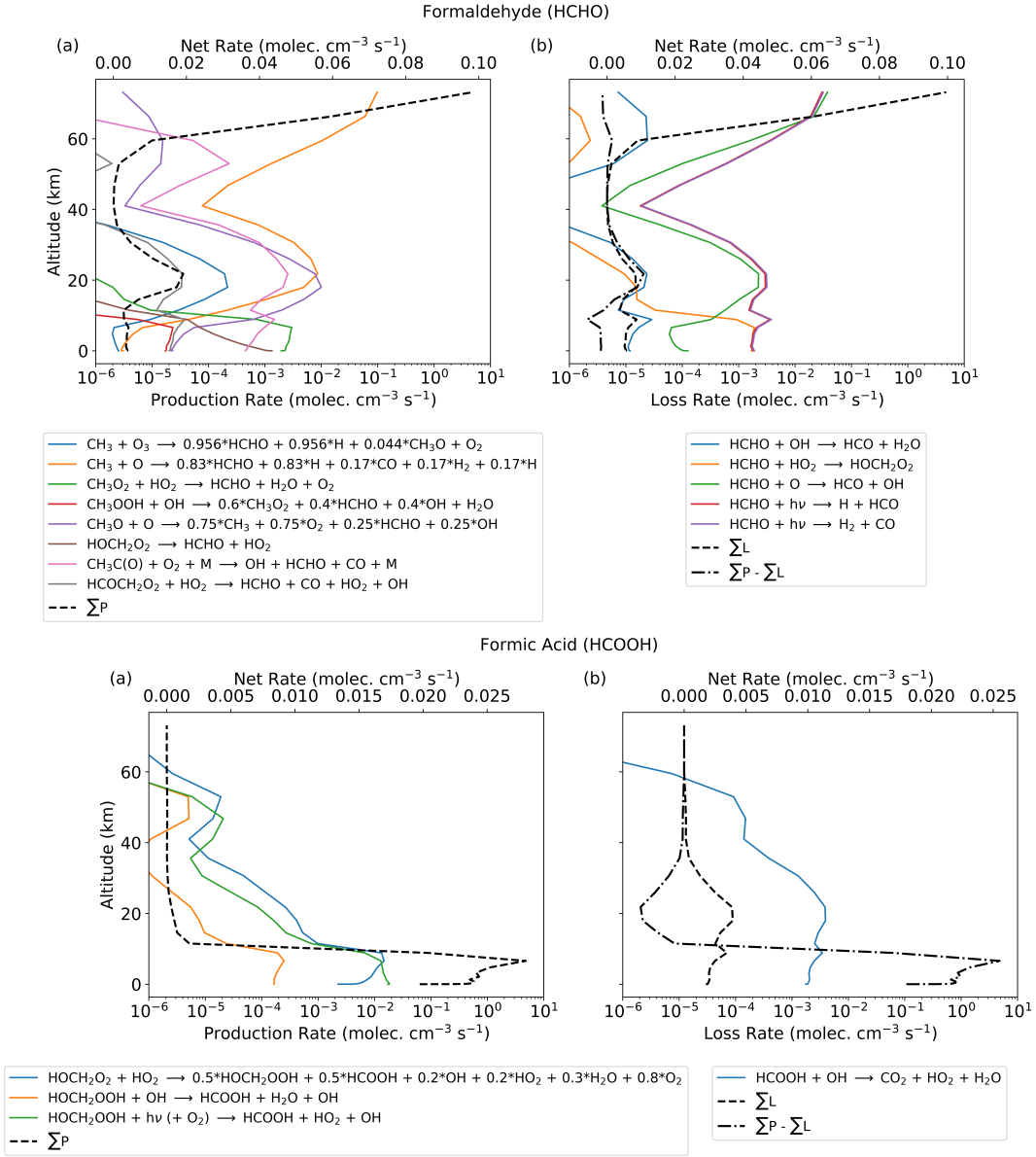

Figure 10. Photochemical production and loss rates (molec cm^{-3}s^{-1}) of HCHO and HCOOH in our 1-D photochemistry model associated with 14 ppb of C_2H_6. Values are for latitude 2.5°N, local time 12:00, and solar longitude 148° as a function of altitude.

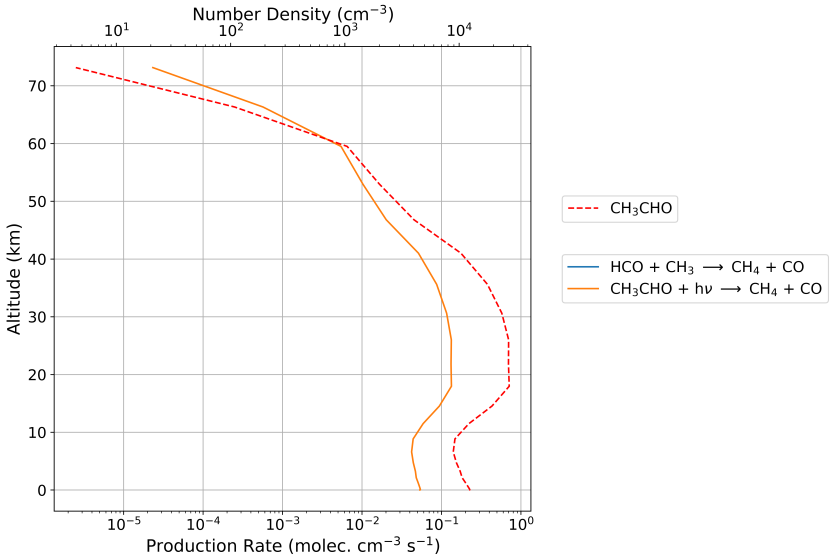

Figure 11. Photochemical production rates of methane (CH_4) from the photolysis of acetaldehyde produced 1 sol after the introduction of the 14 ppb vertically homogeneous distribution of C_2H_6 at latitude 2.5°N, L_S = 148°, LT = 12:00 hrs.

between the north and southern hemisphere throughout the rest of the year, controlled by the sublimation of the respective hemispheres polar caps water ice content.

We find that the photochemical lifetime of C_2H_6 is correlated to the atmospheric water vapour content on Mars. Within the hygropause, lifetimes are found to be within 3–4 years, where OH is the dominant photochemical sink. At higher altitudes, these lifetimes are reduced to 100–400 Mars sols (0.15–0.6 years), due to the higher abundance of atomic oxygen. The lifetimes of acetaldehyde reach values of approximately one sol close to the Martian surface across all equatorial latitudes during the northern spring, that lower to roughly 0.5 sols in the northern hemisphere summer to winter periods. Acetic acid displays a similar seasonal trend, with lifetimes in the northern spring being between 3 and 4 sols below the hygropause , and lowering to between 0.2–1 sol with the elevation of the water saturation point. Oxidation of C_2H_6 in the Martian atmosphere results in a distinct profile of acetaldehyde, as well as greater yields of HCHO and HCOOH, compared to CH_4 oxidation. The 1-D model predicts atmospheric lifetimes of between 15 and 32 hours below altitudes of 25 km during L_S = 0–135°, lowering to 4–12 hours outside of this time frame across all equatorial latitudes, for CH_3CHO. We therefore propose that any instrument detection of CH_3CHO can be attributed to a surface release of C_2H_6 within the immediate local environment of the site of observation.

Our more comprehensive description of atmospheric chemistry, involving 135 organic reactions, significantly expands on the schemes used by Wong and Atreya (2004) and Summers et al. (2002). No formic acid was reported by the model of Wong and Atreya (2004) for their 1-D steady state model with 100 ppm of CH_4, whereas we report concentrations of similar magnitude to HCHO below the hygropause with CH_4 abundances of 14 ppb, a value inspired by V. A. Krasnopolsky (2007). This discrepancy can be explained by our more detailed description of peroxy radical chemistry that is taken from the CAABA/MECCA v4.0 chemistry scheme. In our 1-D model, photochemical lifetimes of HCOOH are inversely proportional to the abundance of OH available. At the top of the hygropause, lifetimes have magnitudes of 1 - 10 sols. Below, the lifetimes vary substantially depending on the water vapour availability. Below 5 km, photochemical life-

times in the drier southern latitudes can reach values exceeding 10^3 sols, whereas in the north, values between 10 and 100 are commonly found. These long photochemical lifetimes of HCOOH, in comparison to HCHO, makes it the most likely photochemical product of CH_4 oxidation that could provide independent verification of CH_4. However, its spectral features do not lie within the NOMAD's spectral range. However, the PFS spectrometer's longwave channel covers a spectral wavenumber range of 250 - 1700 cm^{-1} (Formisano et al., 2005) does span over the position of two absorption features of the HCOOH molecule stored within the High-resolution Transmission Molecular Absorption (HITRAN) database (Gordon et al., 2017).

We find that the introduction of CH_4 at magnitudes similar to reported observations (less than 10^1 ppb) fail to produce perturbations to CO, O_3, or H_2O vapour (not shown) that will be large enough to impact measurements made by solar occultation measurements. CH_4 reactions with $O(^1D)$ above the hygropause and below 50 km has the net effect of increasing OH concentrations by magnitudes of 10^{-1}% after one sol of exposure, which results in catalyzing the conversion of CO to CO_2 via reaction e_1 of B1. The increase in OH arises from the previously described reactions of $O(^1D)$ atoms reacting with CH_4 in the drier altitudes, most notably reaction b_7. CO experiences relative perturbations of -10^{-4}% in the mid-altitudes, which will be lost within instrumental noise. This rise in OH, and the loss of $O(^1D)$ to CH_4 interactions and $O(^3P)$ with organic radical interactions, results in a drop in O_3 production in this region and increased O_3 loss. These perturbations are small, however, with drops of 10^{-1}% after one sol, an amount that will be lost to instrument noise. This highlights that source regions of CH_4 will not be identifiable by perturbations made to inorganic trace gas species observable to the ExoMars Trace Gas Orbiter.

Finally, our model highlights the possible existence of an atmospheric source of CH_4 in the form of C_2H_6 oxidation. The photolysis of acetaldehyde in the Martian atmosphere is capable of producing trace amounts of CH_4 at all altitudes above the Martian surface. Parts per trillion concentrations of CH_3CHO are capable of producing CH_4 at altitudes below 20 km at rates of 10^{-2}–10^{-1} molec cm^{-3} s^{-1} during daylight hours. This could merit further investigation, as biological reactions such as ethylene hydratase (Rosner & Schink, 1995) are capable of converting hydrocarbons below ground to CH_3CHO, which upon exposure to UV radiation may produce abundances of CH_4 greater than 0.02 ppb which could be observable to the TGO instrumentation.

Appendix A Martian Atmospheric Lifetimes of Methane, Formaldehyde, Formic Acid, and Ethane

A1 Methane

Figure A1 shows the net atmospheric lifetime of CH_4, incorporating all loss terms (Figure 2), as a function of latitude and solar longitude. Atmospheric lifetimes reach a minimum of 25–400 year between the top of the hygropause and approximately 50 km due to the larger abundance of the $O(^1D)$ atom. Below the hygropause where OH is the dominant sink, atmospheric lifetimes vary between 400 and 800 years. The longest lifetimes of 800–1600 years lie between 50 and 60 km during winter (L_S = 270-360°), as described above, where the OH and $O(^1D)$ loss processes decline and before photolysis dominates above 60 km.

Variations in atmospheric lifetime are driven by the position of the Martian hygropause and the water vapour content beneath, which is determined by 3-D model output from the MCD (section 2). Water vapour columns reach their maximum during hemispheric summer months when polar water ice sublimates with rising atmospheric temperatures. SPICAM water vapour column measurements at L_S = 50° (Fedorova et al., 2006) show only small variations at latitudes less than 30°, with values ranging from 2–10 pr μm,

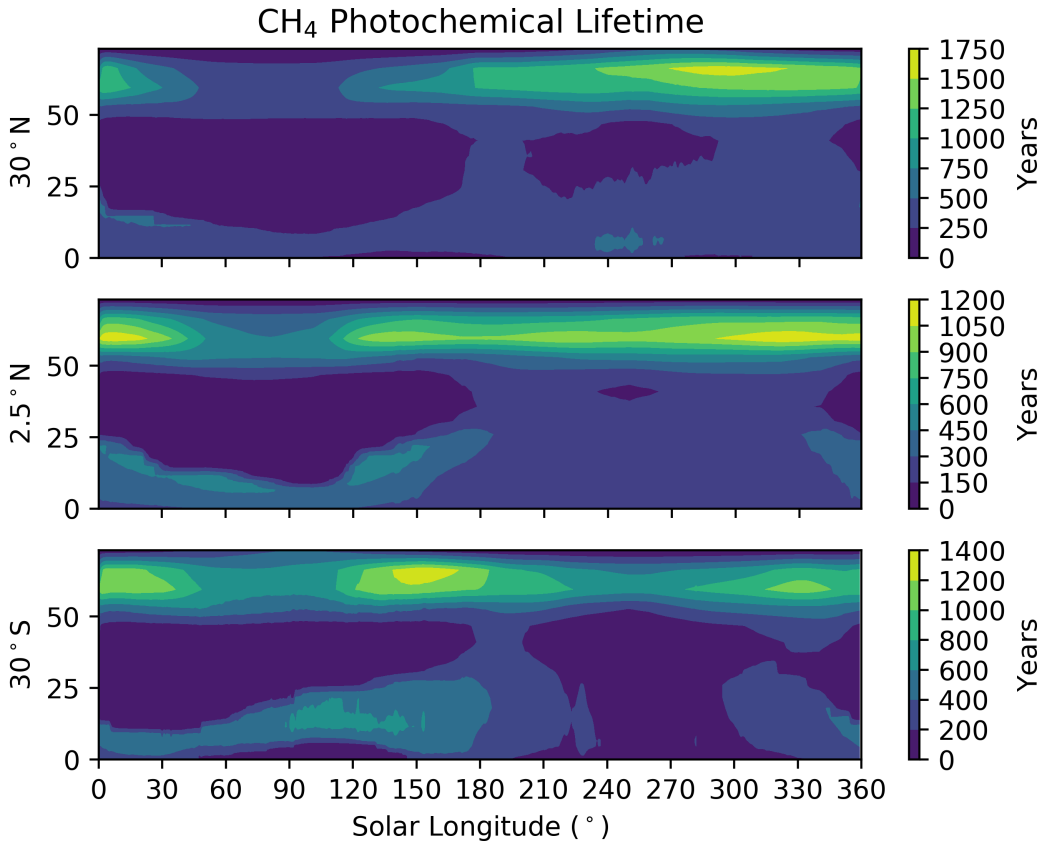

Figure A1. Photochemical lifetime of CH_4 within the atmosphere of Mars and its variations with altitude (km) and solar longitude at latitudes 30°N, 2.5 °N, and 30°S, respectively. All vertical segments are values from the 1-D photochemistry model at 12:00 LT.

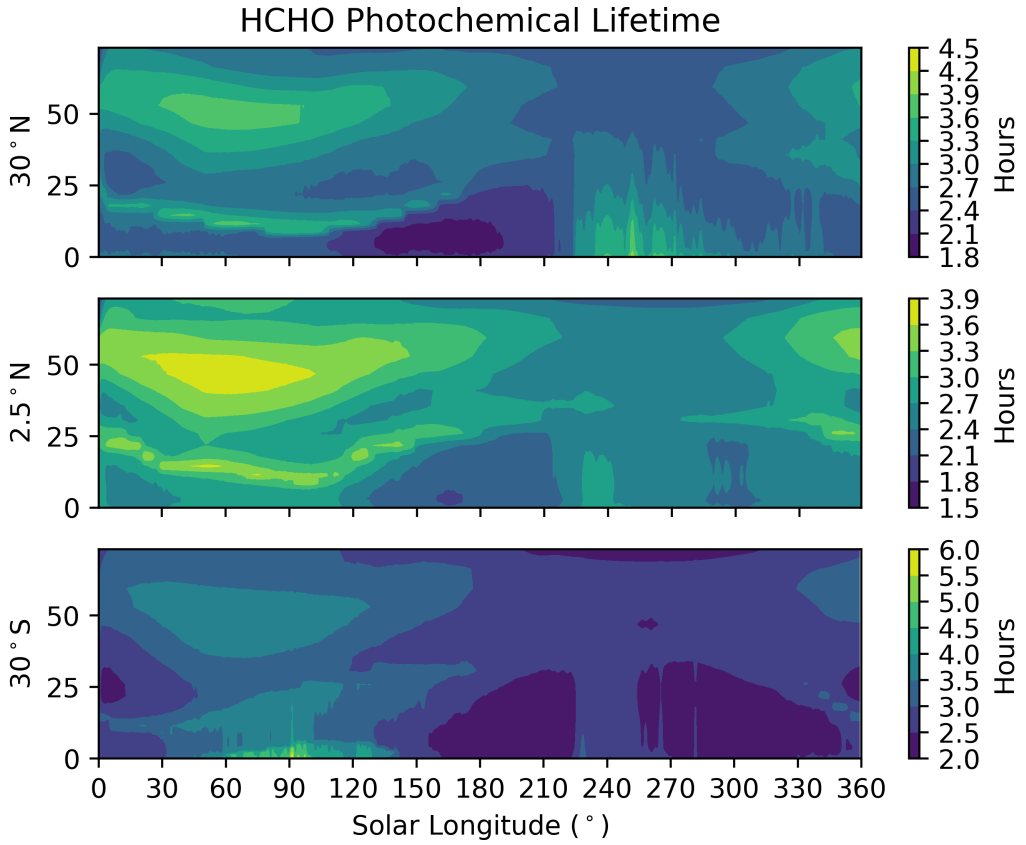

Figure A2. Photochemical lifetime of HCHO within the atmosphere of Mars and its variations with altitude (km) and solar longitude at latitudes 30°N, 2.5 °N, and 30°S, respectively. All vertical segments are values from the 1-D photochemistry model at 12:00 LT.

with saturation values under 25 km. This is consistent with our model loss processes that determine the variation in atmospheric lifetime. Above 50 km, the stronger flux of solar radiation in the northern hemisphere due to the planets axial tilt results in a larger abundance of $O(^1D)$ and a subsequent lower photochemical lifetime of CH_4 than in the southern hemisphere. As water vapour column abundances and saturation altitudes increase with L_S, the low latitude atmospheric lifetime of CH_4 increases below 50 km due to H_2O reacting with $O(^1D)$ and decreases below roughly 25 km. The decrease in solar flux during northern autumn and winter months (L_S = 180°–360°) reduces the production rate of $O(^1D)$ relative to the southern hemisphere, which explains the variation in lifetimes between the hemispheres.

A2 Formaldehyde

Figure A2 shows the resultant seasonal variability of HCHO lifetime at latitudes 30°N, 2.5°N, and 30°S. We find the longest lifetimes, between 4 and 5 hours, are found below 5 km in the southern hemisphere during the northern summer/southern winter, when this region contains low levels of water vapour.

A3 Formic Acid

Figure A3 shows the resultant seasonal variability of HCOOH lifetime at latitudes 30°N, 2.5°N, and 30°S. The lifetime of HCOOH is anti-correlated with water vapour, as expected. The longest lifetime (of magnitude's greater than 10^4 sols) is during the northern spring at altitudes greater than 60 km where OH is lowest. As OH values increase with the supply of water vapour from northern polar ice sublimation, atmospheric lifetimes falls to 1–10 sols close to the hygropause and 10–200 sols at lower altitudes closer to the surface (below 5 km).

With atmospheric lifetimes of this length, describing seasonal changes in HCOOH profiles using a 1-D photochemistry model becomes problematic due to the photochemical lifetimes exceeding the venting timescales associated with our 3.75° thick zonal band that our model represents. Without horizontal transport equations to describe the loss of HCOOH to the zonal band edges, the resultant profiles after a one-year 1-D model run will be subject to gross inaccuracies. As previously discussed in section 2, solving the 1-D model equation for steady state conditions will not yield useful information due to the observed temporal and localized nature of CH_4 emissions, invalidating the notion of a steady-state environment.

A4 Ethane

Figure A4 shows that C_2H_6 has longer photochemical lifetimes below the points of H_2O saturation, where we find typical values that range from 3 to 5 years. In the middle atmosphere, the large abundance of $O(^3P)$ reduced the lifetime to 30–450 sols. Based on these calculations, we suggest that any detection of C_2H_6 made by the TGO instruments will due to an active release.

Appendix B Reaction Rate Coefficients

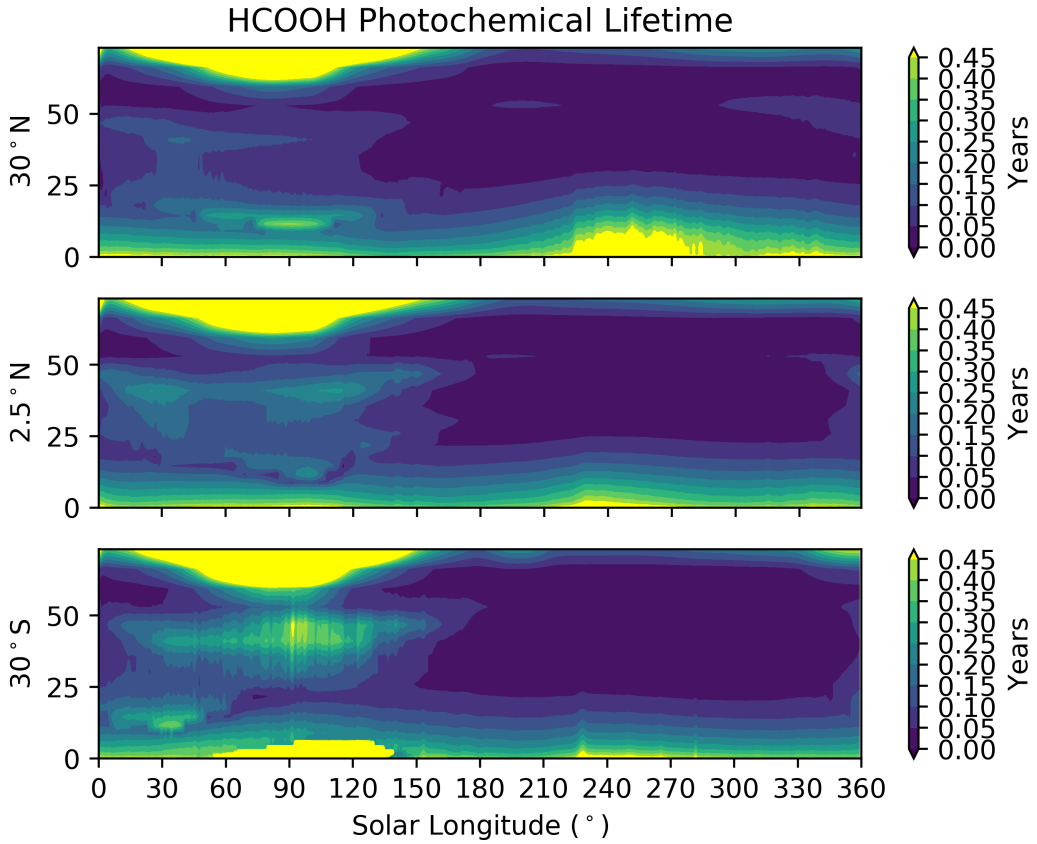

Figure A3. Photochemical lifetime of HCOOH within the atmosphere of Mars and its variations with altitude (km) and solar longitude at latitudes 30°N, 2.5 °N, and 30°S, respectively. All vertical segments are values from the 1-D photochemistry model at 12:00 LT. Contour map saturated for values greater than 0.45 years.

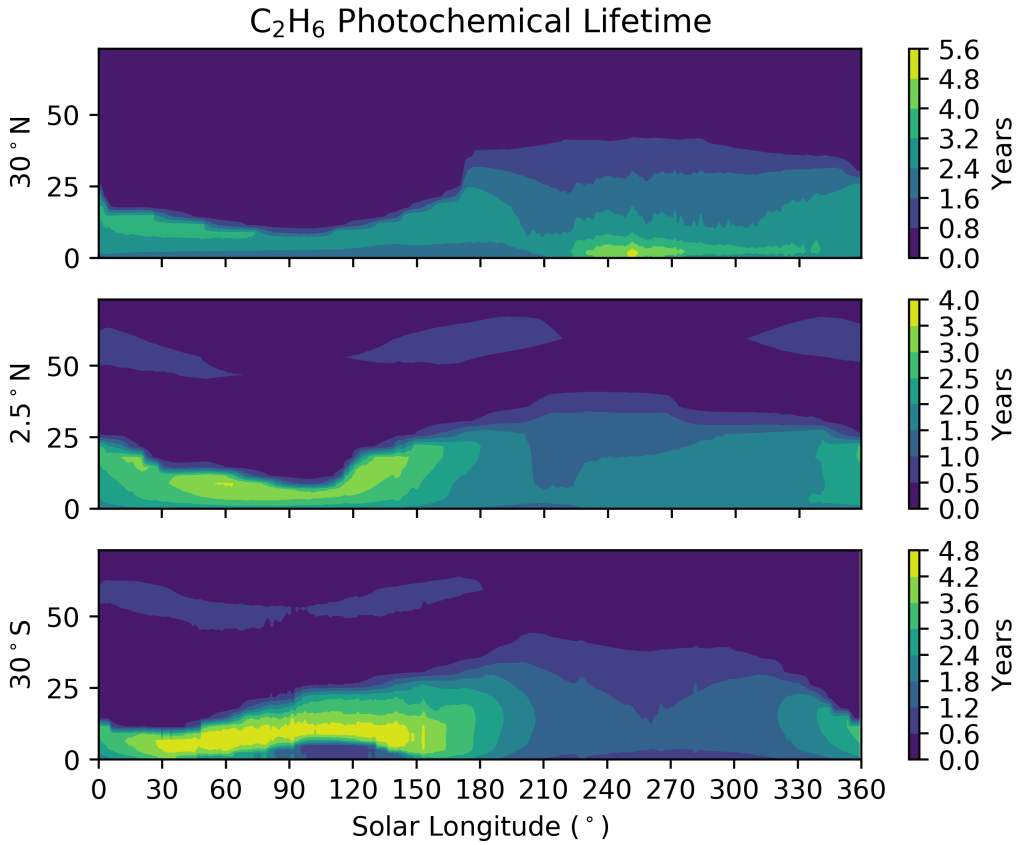

Figure A4. Photochemical lifetime of C_2H_6 within the atmosphere of Mars and its variations with altitude (km) and solar longitude at latitudes 30°N, 2.5 °N, and 30°S, respectively. All vertical segments are values from the 1-D photochemistry model at 12:00 LT.

Table B1. Inorganic reaction rate coefficients within the 1-D photochemistry submodule. Bimolecular rate coefficient units are cm^3 $molec^{-1}$ s^{-1}. Values denoted by superscript *a* are three-body reactions with values taken with atmospheric number density complying to temperatures of T = 298 K and pressures of 660 Pa.

Key	Reaction	Formula	Rate at T = 298 K	Reference
		Reactions with O		
a_1	$O + O_2 + M \rightarrow O_3 + M$	2.075×6.00E-34(T/300)$^{-2.4}$	2.23E-16 [a]	(S. Sander et al., 2003)
a_2	$O + O + M \rightarrow O_2 + M$	2.50×9.46E-34exp(485/T)	2.10E-15 [a]	(Campbell & Gray, 1973)
a_3	$O + O_3 \rightarrow O_2 + O_2$	8.00E-13exp(-2060/T)	7.96E-16	(S. Sander et al., 2003)
		Reactions with O(^{1}D)		
b_1	$O(^1D) + CO_2 \longrightarrow O + CO_2$	7.40E-11exp(120/T)	1.11E-10	(S. Sander et al., 2003)
b_2	$O(^1D) + H_2O \longrightarrow OH + OH$	1.63E-10exp(60/T)	1.99E-10	(S. Sander et al., 2006)
b_3	$O(^1D) + H_2 \longrightarrow OH + H$	1.20E-10	1.20E-10	(S. Sander et al., 2011)
b_4	$O(^1D) + O_2 \longrightarrow O + O_2$	3.30E-11exp(55/T)	3.97E-11	(S. Sander et al., 2006)
b_5	$O(^1D) + O_3 \longrightarrow O_2 + O_2$	1.20E-11	1.20E-11	(S. Sander et al., 2003)
b_6	$O(^1D) + O_3 \longrightarrow O_2 + O + O$	1.20E-11	1.20E-11	(S. Sander et al., 2003)
b_7	$O(^1D) + CH_4 \longrightarrow CH_3 + OH$	0.75×1.75E-10	1.31E-10	(S. Sander et al., 2003)
b_8	$O(^1D) + CH_4 \longrightarrow CH_3O + H$	0.20×1.75E-10	3.50E-11	(S. Sander et al., 2003)
b_9	$O(^1D) + CH_4 \longrightarrow HCHO + H_2$	0.05×1.75E-10	8.75E-12	(S. Sander et al., 2003)
		Reactions with Hydrogen Compounds		
c_1	$O + HO_2 \longrightarrow OH + O_2$	3.00E-11exp(200/T)	5.87E-11	(S. Sander et al., 2003)
c_2	$O + OH \longrightarrow O_2 + H$	1.80E-11exp(180/T)	3.29E-11	(S. Sander et al., 2011)
c_3	$H + O_3 \longrightarrow OH + O_2$	1.40E-10exp(-470/T)	2.89E-11	(S. Sander et al., 2003)
c_4	$H + HO_2 \longrightarrow OH + OH$	7.20E-11	7.20E-11	(S. Sander et al., 2006)
c_5	$H + HO_2 \longrightarrow H_2 + O_2$	6.90E-12	6.90E-12	(S. Sander et al., 2006)
c_6	$H + HO_2 \longrightarrow H_2O + O$	1.60E-12	1.60E-12	(S. Sander et al., 2006)
c_7	$OH + HO_2 \longrightarrow H_2O + O_2$	4.80E-11exp(250/T)	1.11E-10	(S. Sander et al., 2003)
c_8	$HO_2 + HO_2 \longrightarrow H_2O_2O_2$	1.50E-12exp(19/T)	1.60E-12	(Christensen et al., 2002)
c_9	$OH + H_2O_2 \longrightarrow H_2O + HO_2$	1.80E-12	1.80E-12	(S. Sander et al., 2006)
c_{10}	$OH + H_2 \longrightarrow H_2O + H$	2.80E-12exp(-1800/T)	6.67E-15	(S. Sander et al., 2006)
c_{11}	$H + O_2 + M \longrightarrow HO_2 + M$	k_3rd(2.5×4.4E-32, -1.3, 7.5E-11, 0.2)	1.88E-14 [a]	(S. Sander et al., 2011)
c_{12}	$O + H_2O_2 \longrightarrow OH + HO_2$	1.40E-12exp(-2000/T)	1.70E-15	(S. Sander et al., 2003)
c_{13}	$OH + OH \longrightarrow H_2O + O$	1.80E-12	1.80E-12	(S. Sander et al., 2006)
c_{14}	$OH + O_3 \longrightarrow HO_2 + O_2$	1.50E-12exp(-880/T)	7.83E-14	(S. Sander et al., 2003)
c_{15}	$HO_2 + O_3 \longrightarrow OH + O_2 + O_2$	1.00E-14exp(-490/T)	1.93E-15	(S. Sander et al., 2003)
c_{16}	$HO_2 + HO_2 + M \longrightarrow H_2O_2 + O_2 + M$	2.50×2.10E-33exp(920/T)	2.01E-14 [a]	(S. Sander et al., 2011)
c_{17}	$OH + OH + M \longrightarrow H_2O_2 + M$	k_3rd(2.5×6.9E-31,-1, 2.60E-11, 0)	2.70E-13 [a]	(S. Sander et al., 2003)
c_{18}	$H + H + M \longrightarrow H_2 + M$	2.5×1.80E-30/T	2.64E-14 [a]	(Baulch et al., 2005)
		Carbon Compounds		
e_1	$OH + CO \longrightarrow CO_2 + H$	Details in Joshi and Wang (2006)	1.47E-13	(Joshi & Wang, 2006)
e_2	$O + CO + M \longrightarrow CO_2 + M$	2.5×6.50E-33exp(-2184/T)	1.87E-18 [a]	(Tsang & Hampson, 1986)

Table B2. Photolytic reactions of inorganic compounds used within the 1-D photochemistry submodule. Values (s^{-1}) are interpolated from an offline look-up table constructed by a modified TUV (Madronich et al., 2002) model with respect to CO_2 and O_3 column abundances overheard, temperature, optical opacity and solar zenith angle. Values displayed are extracted at zenith conditions, $L_S = 251^\circ$ (perihelion).

Key	Reaction	J(z = 0.50 km)	J(z = 42.67 km)
$j_{O_2 \rightarrow O)}$	$O_2 + h\nu \longrightarrow O + O$	2.95E-10	5.16E-09
$j_{O_2 \rightarrow O(^1D)}$	$O_2 + h\nu \longrightarrow O + O(^1D)$	0	0
$j_{CO_2 \rightarrow O}$	$CO_2 + h\nu \longrightarrow CO + O$	3.79E-12	1.02E-10
$j_{CO_2 \rightarrow O(^1D)}$	$CO_2 + h\nu \longrightarrow CO + O(^1D)$	0	0
$j_{O_3 \rightarrow O(^1D)}$	$O_3 + h\nu \longrightarrow O_2 + O(^1D)$	3.12E-03	4.09E-03
$j_{O_3 \rightarrow O}$	$O_3 + h\nu \longrightarrow O_2 + O$	5.22E-04	6.86E-04
j_{H_2O}	$H_2O + h\nu \longrightarrow H + OH$	1.28E-10	4.67E-08
$j_{H_2O_2}$	$H_2O_2 + h\nu \longrightarrow OH + OH$	3.93E-05	5.26E-05
j_{HO_2}	$HO_2 + h\nu \longrightarrow O + OH$	2.40E-04	3.20E-04

Table B3. Functions and constants used by the R-O_2 permutation reaction handling scheme extracted from the CAABA/MECCA v4.0 box model.

CAABA/MECCA v4.0 Reaction Rate Parameters		
Key	Formula	Notes and Citations
Radical Arrhenius Equations		
k_ch3o2	1.03E-13*exp(365/T)	CH_3O_2 Self-reaction (R. Sander et al., 2019)
k_ch3ooh	5.30E-12*exp(190/T)	CH_3OOH + OH Reaction (R. Sander et al., 2019)
k_ch3co2h	4.00E-14*exp(850/T)	CH_3CO_2H + OH Reaction (R. Sander et al., 2019)
k_ro2ho2_1	2.91E-13*exp(1300/T)*(1 - exp(-0.245*1))	RO_2 + HO_2 (One carbon atom) (R. Sander et al., 2019)
k_ro2ho2_2	2.91E-13*exp(1300/T)*(1 - exp(-0.245*2))	RO_2 + HO_2 (Two carbon atoms) (R. Sander et al., 2019)
Arrhenius Equations for H Abstraction by OH		
k_s	4.50E-18*T^2*exp(253./T)	(Taraborrelli, 2010; R. Sander et al., 2019)
k_t	2.12E-18*T^2*exp(696/T)	(Taraborrelli, 2010; R. Sander et al., 2019)
k_rohro	2.10E-18*T^2*exp(-85/T)	(Taraborrelli, 2010; R. Sander et al., 2019)
k_roohro	0.60*k_ch3ooh	(Taraborrelli, 2010; R. Sander et al., 2019)
k_co2h	0.7*k_ch3co2h	(Taraborrelli, 2010; R. Sander et al., 2019)
kdec	1.00E6	(Atkinson et al., 2006; R. Sander et al., 2019)
Updated Rate Constants for RO_3 + HO_2 Reactions		
kapho2	5.20E-13*exp(980/T)*1.865	(Groß et al., 2014; R. Sander et al., 2019)
Arrhenius Equations for Permutation Reactions		
k_ro2soro2	2*(7.70E-15*exp(1330/T)*k_ch3o2)$^{0.5}$	(R. Sander et al., 2019)
k_ro2rco3	4.00E-12*exp(500/T)	(R. Sander et al., 2019)
k_ro2poro2	2*7.50E-14*exp(500/T)	(R. Sander et al., 2019)
Substituent Factors		
f_soh	3.44	(Taraborrelli, 2010; R. Sander et al., 2019)
f_sooh	8.00	(Taraborrelli, 2010; R. Sander et al., 2019)
f_pch2oh	1.29	(Taraborrelli, 2010; R. Sander et al., 2019)
f_tooh	8.00	(Taraborrelli, 2010; R. Sander et al., 2019)
f_toh	2.68	(Taraborrelli, 2010; R. Sander et al., 2019)
f_o	8.15	(Taraborrelli, 2010; R. Sander et al., 2019)
f_cho	0.55	(Taraborrelli, 2010; R. Sander et al., 2019)
f_co2h	1.67	(Taraborrelli, 2010; R. Sander et al., 2019)
Branching Ratios for RO_2 + HO_2 Reactions		
rco3_o3	0.10	(Groß et al., 2014; R. Sander et al., 2019)
rco3_oh	0.69	(Groß et al., 2014; R. Sander et al., 2019)
rco3_ooh	0.21	(Groß et al., 2014; R. Sander et al., 2019)
rchoch2o2_oh	0.10	(R. Sander et al., 2019)
rcoch2o2_oh	0.15	(R. Sander et al., 2019)
rcoch2o2_ooh	0.85	(R. Sander et al., 2019)

Table B4. Chemical reactions and rate coefficients involved in the oxidation of CH_4 used in our 1-D photochemistry model. Bimolecular rate coefficient units are cm^3 $molec^{-1}$ s^{-1}. [a] are three-body reactions with values taken with atmospheric number density complying to temperatures of T = 298 K and pressures of 660 Pa. [b] are unimolecular rate coefficients with units s^{-1}.

Methane Reaction Scheme				
Key	Reaction	Formula	Rate at T = 298 K	Reference
cab_1	$CH_4 + OH \longrightarrow CH_3 + OH$	1.85E-20exp(2.82LOG(T) - 987./T)	6.40E-15	(R. Sander et al., 2019)
cab_2	$CH_4 + O \longrightarrow 0.51 * CH_3 + 0.51 * OH$ $+0.49 * CH_3O + 0.49 * H$	6.03E-18($T^{2.17}$)exp(-3619/T)	7.50E-18	(R. Sander et al., 2019)
cab_3	$CH_3 + O_2 + M \longrightarrow CH_3O_2 + M$	k_3rd(7.00E-31, 3., 1.80E-12, -1.1)	1.14E-13 [a]	(R. Sander et al., 2019)
cab_4	$CH_3 + O_3 \longrightarrow 0.956 * HCHO + 0.956 * H$ $+0.044 * CH_3O + O_2$	5.10E-12exp(-210/T)	2.52E-12	(R. Sander et al., 2019)
cab_5	$CH_3 + O \longrightarrow 0.83 * HCHO + 0.83 * H$ $+0.17 * CO + 0.17 * H_2 + 0.17 * H$	1.30E-10	1.3E-10	(R. Sander et al., 2019)
cab_6	$CH_3O_2 + HO_2 \longrightarrow CH_3OOH + O_2$	3.8E-13exp(780/T) /(1 + 1/(498exp(1160/T)))	5.21E-12	(R. Sander et al., 2019)
cab_7	$CH_3O_2 + HO_2 \longrightarrow HCHO + H_2O + O_2$	3.8E-13exp(780/T) /(1 + 498exp(-1160/T)))	4.67E-13	(R. Sander et al., 2019)
cab_8	$CH_3O_2 + R - O_2 \longrightarrow CH_3O + 0.5 * O_2$	2×7.40E-13exp(-520/T)	2.59E-13	(R. Sander et al., 2019)
cab_9	$CH_3O_2 + R - O_2 \longrightarrow 0.5 * HCHO$ $+0.5 * CH_3OH + 0.5 * O_2$	2×(k_ch3o2 - 7.40E-13exp(-520/T))	4.43E-13	(R. Sander et al., 2019)
cab_{10}	$CH_3O_2 + O_3 \longrightarrow CH_3O + O_2 + O_2$	2.90E-16exp(-1000/T)	1.01E-17	(R. Sander et al., 2019)
cab_{11}	$CH_3O_2 + OH \longrightarrow CH_3O + HO_2$	1.40E-10	1.40E-10	(R. Sander et al., 2019)
cab_{12}	$CH_3O_2 + O \longrightarrow CH_3O + O_2$	4.30E-11	4.30E-11	(R. Sander et al., 2019)
cab_{13}	$CH_3OH + OH \longrightarrow 0.85 * HCHO$ $+0.85 * HO_2 + 0.15 * CH_3O + H_2O$	6.38E-18(T^2)exp(144/T)	9.19E-13	(R. Sander et al., 2019)
cab_{14}	$CH_3OOH + OH \longrightarrow 0.6 * CH_3O_2$ $+0.4 * HCHO + 0.4 * OH + H_2O$	k_ch3ooh_oh	1.00E-11	(R. Sander et al., 2019)
cab_{15}	$CH_3O + O_2 \longrightarrow HO_2 + HCHO$	1.30E-14exp(-633/T)	1.55E-15	(R. Sander et al., 2019)
cab_{16}	$CH_3O + O_3 \longrightarrow CH_3O_2 + O_2$	2.53E-14	2.53E-14	(R. Sander et al., 2019)
cab_{17}	$CH_3O + O \longrightarrow 0.75 * CH_3 + 0.75 * O_2$ $+0.25 * HCHO + 0.25 * OH$	2.50e-11	2.50E-11	(R. Sander et al., 2019)
cab_{18}	$HCHO + OH \longrightarrow HCO + H_2O$	5.50E-12exp(-125/T)	3.60e-12	(S. Sander et al., 2011)
cab_{19}	$HCHO + HO_2 \longrightarrow HOCH_2O_2$	9.70E-15exp(625/T)	7.90E-14	(R. Sander et al., 2019)
cab_{20}	$HCHO + O \longrightarrow HCO + OH$	2.99E-11exp(-1529/T)	1.77E-13	(Herron, 1988)
cab_{21}	$HCO + O \longrightarrow CO + OH$	5.00E-11	5.00E-11	(Baulch et al., 1992)
cab_{22}	$HCO + CH_3 \longrightarrow CH_4 + CO$	4.40E-11	4.40E-11	(S. Mulenko, 1987)
cab_{23}	$HCO + CH_3 \longrightarrow CH_3CHO$	4.42E-11	4.42E-11	(S. A. Mulenko, 1980)
cab_{24}	$HCO + HCO \longrightarrow HCHO + CO$	4.48E-11	4.48E-11	(Friedrichs et al., 2002)
cab_{25}	$HCO + OH \longrightarrow CO + H_2O$	1.69E-10	1.69E-10	(Baulch et al., 1992)
cab_{26}	$HCO + O_2 \longrightarrow CO + HO_2$	5.20E-12	5.20E-12	(S. Sander et al., 2011)
cab_{27}	$HCO + H \longrightarrow CO + H_2$	1.83E-10	1.83E-10	(Friedrichs et al., 2002)
cab_{28}	$HOCH_2O_2 \longrightarrow HCHO + HO_2$	2.40E12exp(-7000/T)	150.89 [b]	(R. Sander et al., 2019)
cab_{29}	$HOCH_2O_2 + HO_2 \longrightarrow 0.5 * HOCH_2OOH$ $+0.5 * HCOOH + 0.2 * OH + 0.2 * HO_2 + 0.3 * H_2O + 0.8 * O_2$	5.6E-15exp(2300/T)	1.26E-12	(R. Sander et al., 2019)
cab_{30}	$HOCH_2O_2 + R - O_2 \longrightarrow HCOOH + HO_2$	2×(k_ch3o2×5.50E-12)$^{0.5}$	2.78E-12	(R. Sander et al., 2019)
cab_{31}	$HOCH_2O_2 + R - O_2 \longrightarrow 0.5 * HCOOH$ $+0.5 * HOCH_2OH + 0.5 * O_2$	2×(k_ch3o2×5.70E-14 ×exp(750/T))$^{0.5}$	9.95E-13	(R. Sander et al., 2019)
cab_{32}	$HCOOH + OH \longrightarrow CO_2 + HO_2 + H_2O$	2.94E-14exp(786/T) + 9.85E-13exp(-1036/T)	4.42E-13	(R. Sander et al., 2019)
cab_{33}	$HOCH_2OOH + OH \longrightarrow HOCH_2O_2$	k_roohro	6.02E-12	(R. Sander et al., 2019)
cab_{34}	$HOCH_2OOH + OH \longrightarrow HCOOH + H_2O + OH$	k_rohro + k_s×f_soh×f_sooh	2.59E-11	(R. Sander et al., 2019)
cab_{35}	$HOCH_2OH + OH \longrightarrow HO_2 + HCOOH + H_2O$	2×k_rohro + k_s×f_soh^2	1.13E-11	(R. Sander et al., 2019)

Table B5. Chemical reactions and rate coefficients involved in the oxidation of C_2H_6 used in our 1-D photochemistry model. Bimolecular rate coefficient units are cm^3 $molec^{-1}$ s^{-1}. [a] are three-body reactions with values taken with atmospheric number density complying to temperatures of T = 298 K and pressures of 660 Pa. [b] are unimolecular rate coefficients with units s^{-1}.

Ethane Reaction Scheme				
Key	Reaction	Formula	Rate at T = 298 K	Reference
cab_{36}	$C_2H_6 + OH \longrightarrow C_2H_5 + H_2O$	7.66E-12exp(-1020/T)	2.50E-13	(S. Sander et al., 2011)
cab_{37}	$C_2H_6 + O \longrightarrow C_2H_5 + OH$	2.21E-15(T/298)$^{6.5}$exp(-132/T)	1.42E-15	(Cohen & Westberg, 1991)
cab_{38}	$CH_3 + CH_3 + M \longrightarrow C_2H_6$	Details in (Cody et al., 2003)	5.12E-11 [a]	(Cody et al., 2003)
cab_{39}	$C_2H_5 + O_2 + M \longrightarrow C_2H_5O_2$	2.5×1.50E-28(298/T)^3×dens	6.02E-11 [a]	(S. Sander et al., 2011)
cab_{40}	$C_2H_5 + C_2H_5 \longrightarrow C_2H_4 + C_2H_6$	2.01E-12	2.01E-12	(Dobis & Benson, 1991)
cab_{41}	$C_2H_5 + O_2 \longrightarrow C_2H_4 + HO_2$	1.90E-14	1.90E-14	(S. Sander et al., 2011)
cab_{42}	$C_2H_5 + H \longrightarrow CH_3 + CH_3$	7.95E-11exp(-132/T)	5.11E-11	(Pratt & Wood, 1984)
cab_{43}	$C_2H_5O_2 + HO_2 \longrightarrow C_2H_5OOH + O_2$	7.50E-13exp(700/T)	7.86E-12	(R. Sander et al., 2019)
cab_{44}	$C_2H_5O_2 + RO_2 \longrightarrow 0.8 * CH_3CHO + 0.6 * HO_2 + 0.2 * C_2H_5OH + O_2$	2(7.60E-14*k_ch3o2)$^{0.5}$	3.27E-13	(R. Sander et al., 2019)
cab_{45}	$C_2H_5OOH + HO_2 \longrightarrow C_2H_5OOH + O_2$	k_roohro	6.02E-12	(R. Sander et al., 2019)
cab_{46}	$C_2H_5OOH + OH \longrightarrow CH_3CHO + OH$	k_s*f_sooh	7.47E-12	(R. Sander et al., 2019)
cab_{47}	$C_2H_5OH + OH \longrightarrow 0.95 * C_2H_5O_2 + 0.95 * HO_2 + 0.05 * HOCH_2CH_2O_2 + H_2O$	3.00E-12exp(20/T)	3.21E-12	(R. Sander et al., 2019)
cab_{48}	$HOCH_2CH_2O_2 + RO_2 \longrightarrow 0.6 * HOCH_2CH_2O + 0.2 * HOCH_2CHO + 0.2 * ETHGLY$	2*(7.80E-14exp(1000/T)*k_ch3o2)$^{0.5}$	1.77E-12	(R. Sander et al., 2019)
cab_{49}	$HOCH_2CH_2O_2 + HO_2 \longrightarrow HYETHO2H$	1.53E-13exp(1300/T)*(1-k_rchohch2o2_oh)	1.08E-11	(R. Sander et al., 2019)
cab_{50}	$HOCH_2CH_2O_2 + HO_2 \longrightarrow HOCH_2CH_2O + OH$	1.53E-13exp(1300/T)*k_rchohch2o2_oh	1.20E-12	(R. Sander et al., 2019)
cab_{51}	$HOCH_2CH_2O + O_2 \longrightarrow HO_2 + HOCH_2CHO$	6.00E-14exp(-550/T)	9.48E-15	(R. Sander et al., 2019)
cab_{52}	$HOCH_2CH_2O \longrightarrow HO_2 + HCHO + HCHO$	9.5E13exp(-5988/T)	1.78E5 [b]	(R. Sander et al., 2019)
cab_{53}	$ETHGLY + OH \longrightarrow HOCH_2CHO + HO_2 + H_2O$	2*k_s*f_soh*f_pch2oh + 2*k_rohro	8.57E-12	(R. Sander et al., 2019)
cab_{54}	$HYETHO2H + OH \longrightarrow HOCH_2CH_2O_2 + H_2O$	k_roohro	6.02E-12	(R. Sander et al., 2019)
cab_{55}	$HYETHO2H + OH \longrightarrow HOCH_2CHO + OH + H_2O$	k_s*f_sooh*f_pch2oh	9.64E-12	(R. Sander et al., 2019)
cab_{56}	$HYETHO2H + OH \longrightarrow HOOCH_2CHO + HO_2 + H_2O$	k_s*f_soh*f_pch2oh + k_rohro	4.29E-12	(R. Sander et al., 2019)
cab_{57}	$CH_3CHO + OH \longrightarrow CH_3C(O) + H_2O$	4.40E-12exp(365/T)*0.95	1.42E-11	(R. Sander et al., 2019)
cab_{58}	$CH_3CHO + OH \longrightarrow HCOCH_2O_2 + H_2O$	4.40E-12exp(365/T)*0.05	7.48e-13	(R. Sander et al., 2019)
cab_{59}	$CH_3CHO + HO_2 \longrightarrow CH_3CHOHO_2$	3.46E12exp(-12500/(1.98*T)) / 6.34E26*exp(-1470/(1.98*T))	4.77E-22	(R. Sander et al., 2019)
cab_{60}	$CH_3CHO + HCOOH \longrightarrow CH_2CHOH + HCOOH$	(1.17E-19*T$^{2.209}$)exp(-556/(1.987T))	1.34E-14	(R. Sander et al., 2019)
cab_{61}	$CH_2CHOH + OH \longrightarrow HCOOH + OH + HCHO$	4.30E-11	4.30E-11	(R. Sander et al., 2019)
cab_{62}	$CH_2CHOH + OH \longrightarrow HOCH_2CHO + HO_2$	2.40E-11	2.40E-11	(R. Sander et al., 2019)
cab_{63}	$CH_2CHOH + HCOOH \longrightarrow CH_3CHO + HCOOH$	(4.67E-26*T$^{3.286}$)exp(-556/(T*1.987))	2.47E-18	(R. Sander et al., 2019)
cab_{64}	$CH_3CHOHO_2 \longrightarrow CH_3CHO + HO_2$	3.46E12exp(-12500/(T*1.98))	2.18E3 [b]	(R. Sander et al., 2019)
cab_{65}	$CH_3CHOHO_2 + HO_2 \longrightarrow 0.5 * CH_3CHOHOOH + 0.3 * CH_3COOH + 0.2 * CH_3 + 0.2 * HCOOH + 0.2 * OH + O_2$	5.60E-15exp(2300/T)	1.26E-11	(R. Sander et al., 2019)
cab_{66}	$CH_3CHOHO_2 + RO_2 \longrightarrow CH_3 + HCOOH + OH$	k_ro2soro2	9.68E-13	(R. Sander et al., 2019)
cab_{67}	$CH_3COOH + OH \longrightarrow CH_3 + CO_2 + H_2O$	4.00E-14exp(850/T)	6.93E-13	(R. Sander et al., 2019)
cab_{68}	$CH_3CHOHOOH + OH \longrightarrow CH_3COOH + OH$	k_t*f_tooh*f_toh + k_rohro	4.19E-11	(R. Sander et al., 2019)
cab_{69}	$CH_3CHOHOOH + OH \longrightarrow CH_3CHOHO_2$	k_roohro	6.02E-12	(R. Sander et al., 2019)
cab_{70}	$CH_3C(O) + O_2 + M \longrightarrow CH_3C(O)OO + M$	5.10E-12(1 - 1/(1 + 9.48E-18*dens*2.5))	4.04E-12 [a]	(R. Sander et al., 2019)
cab_{71}	$CH_3C(O) + O_2 + M \longrightarrow OH + HCHO + CO + M$	5.10E-12/(1 + 9.48E-18*dens*2.5))	1.06E-12 [a]	(R. Sander et al., 2019)
cab_{72}	$CH_3C(O)OO + HO_2 \longrightarrow OH + CH_3 + CO_2$	5.20E-13exp(980/T)*1.507*0.61	1.28E-11	(R. Sander et al., 2019)
cab_{73}	$CH_3C(O)OO + HO_2 \longrightarrow CH_3C(O)OOH$	5.20E-13exp(980/T)*1.507*0.23	4.83E-12	(R. Sander et al., 2019)
cab_{74}	$CH_3C(O)OO + HO_2 \longrightarrow CH_3COOH + O_3$	5.20E-13exp(980/T)*1.507*0.16	3.36E-12	(R. Sander et al., 2019)
cab_{75}	$CH_3C(O)OO + RO_2 \longrightarrow CH_3 + CO_2$	k_ro2rco3*0.9	1.93E-11	(R. Sander et al., 2019)
cab_{76}	$CH_3C(O)OO + RO_2 \longrightarrow CH_3COOH$	k_ro2co3*0.1	2.14E-12	(R. Sander et al., 2019)
cab_{77}	$CH_3C(O)OOH + OH \longrightarrow CH_3C(O)OO + H_2O$	k_roohro	6.02E-12	(R. Sander et al., 2019)
cab_{78}	$HCOCH_2O_2 + RO_2 \longrightarrow 0.6 * HCHO + 0.6 * CO + 0.6 * HO_2 + 0.2 * GLYOX + 0.2 * HOCH_2CHO$	k_ro2poro2	8.03E-12	(R. Sander et al., 2019)
cab_{79}	$HCOCH_2O_2 + HO_2 \longrightarrow HOOCH_2CHO$	k_ro2ho2_2*rcoch2o2_ooh	7.52E-12	(R. Sander et al., 2019)
cab_{80}	$HCOCH_2O_2 + HO_2 \longrightarrow HCHO + CO + HO_2 + OH$	k_ro2ho2_2*rcoch2o2_oh	1.33E-12	(R. Sander et al., 2019)
cab_{81}	$GLYOX + OH \longrightarrow HCOCO + H_2O$	3.10E-12exp(340/T)	9.70E-12	(R. Sander et al., 2019)
cab_{82}	$HCOCO \longrightarrow HCO + CO$	1.40E12exp(-3159/T)	3.54E7 [b]	(Orlando & Tyndall, 2001)
cab_{83}	$HCOCO + O_2 \longrightarrow HCOCO_3$	5.00E-12*3.2*exp(-550/T)	2.53E-12	(R. Sander et al., 2019)
cab_{84}	$HCOCO + O_2 \longrightarrow OH + CO + CO_2$	5.00E-12(1 - 3.2exp(-550/T))	2.47E-12	(R. Sander et al., 2019)
cab_{85}	$HOOCH_2CHO + OH \longrightarrow HCOCH_2O_2 + H_2O$	k_roohro	6.02E-12	(R. Sander et al., 2019)
cab_{86}	$HOOCH_2CHO + OH \longrightarrow HCHO + CO + OH + H_2O$	0.8*8.00E-12	6.40E-12	(R. Sander et al., 2019)
cab_{87}	$HOOCH_2CHO + OH \longrightarrow GLYOX + OH + H_2O$	0.55*k_s*f_sooh*f_cho	2.26E-12	(R. Sander et al., 2019)
cab_{88}	$HOCH_2CHO + OH \longrightarrow HOCH_2CO + H_2O$	0.8*8.00E-12	6.40E-12	(R. Sander et al., 2019)
cab_{89}	$HOCH_2CHO + OH \longrightarrow HOCHCHO + H_2O$	0.2*8.00E-12	1.60E-12	(R. Sander et al., 2019)
cab_{90}	$HOCHCHO \longrightarrow GLYOX + HO_2$	kdec	1.00E6 [b]	(R. Sander et al., 2019)
cab_{91}	$HOCH_2CO + O_2 + M \longrightarrow HOCH_2CO_3 + M$	5.10E-12*(1 - 1/(1 + 1.85E-18*dens*2.5))	2.17E-12 [a]	(R. Sander et al., 2019)
cab_{92}	$HOCH_2CO + O_2 + M \longrightarrow OH + HCHO + CO_2 + M$	5.10E-12*(1 + 1.85E-18*dens*2.5)	8.89E-12 [a]	(R. Sander et al., 2019)
cab_{93}	$HOCH_2CO_3 + RO_2 \longrightarrow HCHO + CO_2 + HO_2$	k_ro2rco3*0.9	1.93E-11	(R. Sander et al., 2019)
cab_{94}	$HOCH_2CO_3 + RO_2 \longrightarrow HOCH_2CO_2H$	k_ro2rco3*0.1	2.14E-12	(R. Sander et al., 2019)
cab_{95}	$HOCH_2CO_3 + HO_2 \longrightarrow HCHO + OH + HO_2 + CO_2$	kapho2*rco3_oh	9.25E-12	(R. Sander et al., 2019)
cab_{96}	$HOCH_2CO_3 + HO_2 \longrightarrow HOCH_2CO_3H$	kapho2*rco3_ooh	2.82E-12	(R. Sander et al., 2019)
cab_{97}	$HOCH_2CO_3 + HO_2 \longrightarrow HOCH_2CO_2H + O_3$	kapho2*rco3_o3	1.34E-12	(R. Sander et al., 2019)
cab_{98}	$HOCH_2CO_2H + OH \longrightarrow 0.09 * HCHO + 0.91 * HCOCO_2H + HO_2 + H_2O$	k_co2h + k_s*f_soh*f_co2h	5.50E012	(R. Sander et al., 2019)
cab_{99}	$HCOCO_2H + OH \longrightarrow CO + HO_2 + CO_2 + H_2O$	k_co2h + k_t*f_o*f_co2h	2.66E-11	(R. Sander et al., 2019)
cab_{100}	$HOCH_2CO_3H + OH \longrightarrow HOCH_2CO_3 + H_2O$	k_roohro	6.02E-12	(R. Sander et al., 2019)
cab_{101}	$HOCH_2CO_3H + OH \longrightarrow HCOCO_3H + HO_2$	k_s*f_soh*f_co2h	5.37E-12	(R. Sander et al., 2019)
cab_{102}	$HCOCO_3H + OH \longrightarrow HCOCO_3 + H_2O$	k_roohro	6.02E-12	(R. Sander et al., 2019)
cab_{103}	$HCOCO_3H + OH \longrightarrow CO + CO_2 + H_2O + OH$	k_t*f_o*f_co2h	2.65E-11	(R. Sander et al., 2019)
cab_{104}	$HCOCO_3 + RO_2 \longrightarrow CO + HO_2 + CO_2$	k_ro2rco3*0.9	1.93E-11	(R. Sander et al., 2019)
cab_{105}	$HCOCO_3 + RO_2 \longrightarrow HCOCO_2H + O_2$	k_ro2rco3*0.1	2.14E-12	(R. Sander et al., 2019)
cab_{106}	$HCOCO_3 + HO_2 \longrightarrow HO_2 + CO + CO_2 + OH$	kapho2	1.34E-11	(R. Sander et al., 2019)

Table B6. Organic photolytic reactions used within the 1-D photochemistry submodule. Values (s^{-1}) are interpolated from an offline look-up table constructed by a modified TUV (Madronich et al., 2002) model with respect to CO_2 and O_3 column abundances overheard, temperature, optical opacity and solar zenith angle. Values displayed are extracted at zenith conditions, $L_S = 251^\circ$ (perihelion).

Key	Reaction	J(z = 0.50 km)	J(z = 42.67 km)	J(z = 69.81 km)
$j_{CH_4 \rightarrow CH_3}$	$CH_4 + h\nu \longrightarrow CH_3 + H$	0.00	0.00	8.12E-10
$j_{CH_4 \rightarrow {}^1CH_2}$	$CH_4 + h\nu \longrightarrow {}^1CH_2 + H_2$	0.00	0.00	1.63E-9
$j_{CH_4 \rightarrow {}^3CH_2}$	$CH_4 + h\nu \longrightarrow {}^3CH_2 + H + H$	0.00	0.00	1.53E-10
$j_{CH_4 \rightarrow CH}$	$CH_4 + h\nu \longrightarrow CH + H_2 + H$	0.00	0.00	1.95E-10
j_{CH_3OOH}	$CH_3OOH + h\nu \longrightarrow CH_3O + OH$	2.23E-5	2.90E-5	2.97E-5
$j_{HCHO \rightarrow HCO}$	$HCHO + h\nu \longrightarrow HCO + H$	3.54E-5	4.62E-5	4.74E-5
$j_{HCHO \rightarrow CO}$	$HCHO + h\nu \longrightarrow H_2 + CO$	3.71E-5	4.88E-5	5.01E-5
j_{CH_3OH}	$CH_3OH + h\nu \longrightarrow CH_3O + H$	1.59E-7	1.12E-6	1.64E-6
$j_{C_2H_6}$	$C_2H_6 + h\nu \longrightarrow Products$	0.00	0.00	2.39E-9
$j_{CH_3CHO \rightarrow CH_3}$	$CH_3CHO + h\nu \longrightarrow CH_3 + HCO$	2.43E-5	3.40E-5	3.44E-5
$j_{CH_3CHO \rightarrow CH_4}$	$CH_3CHO + h\nu \longrightarrow CH_4 + CO$	5.46E-6	6.80E-6	6.81E-6
j_{HOCH_2OOH}	$HOCH_2OOH + h\nu(+O_2) \longrightarrow HCOOH + HO_2 + OH$	4.43E-5	5.43E-5	5.43E-5
$j_{HOCH_2CHO \rightarrow HCO}$	$HOCH_2CHO + h\nu \longrightarrow CH_3O + HCO$	4.08E-5	5.04E-5	5.05E-5
$j_{HOCH_2CHO \rightarrow CO}$	$HOCH_2CHO + h\nu \longrightarrow CH_3OH + CO$	4.91E-6	6.07E-6	6.09E-6
$j_{HOCH_2CHO \rightarrow OH}$	$HOCH_2CHO + h\nu(+O_2) \longrightarrow HCOCH_2O_2 + OH$	3.44E-6	4.25E-6	4.26E-6
$j_{Glyox \rightarrow HCO}$	$Glyoxal + h\nu \longrightarrow HCO + HCO$	7.84E-5	8.49E-5	8.5E-5
$j_{Glyox \rightarrow H_2}$	$Glyoxal + h\nu \longrightarrow H_2 + CO + CO$	1.90E-5	2.19E-5	2.20E-5
$j_{Glyox \rightarrow HCHO}$	$Glyoxal + h\nu \longrightarrow HCHO + CO$	2.79E-5	3.13E-5	3.14E-5
j_{CH_3COOH}	$CH_3COOH + h\nu \longrightarrow CH_3 + COOH$	7.77E-6	9.43E-6	9.44E-6
$j_{CH_3C(O)OOH}$	$CH_3C(O)OOH + h\nu \longrightarrow CH_3 + OH + CO_2$	3.85E-5	4.73E-6	4.75E-5

Proxies			
Key	Reaction	Proxy	Source
$j_{HOCH_2CO_3H}$	$HOCH_2CO_3H + h\nu \longrightarrow HCHO + HO2 + OH + CO2$	j_{CH_3OOH}	(R. Sander et al., 2014)
j_{HCOCO_2H}	$HCOCO_2H + h\nu \longrightarrow 2HO_2 + CO + CO_2$	$3.95 \times j_{HCHO \rightarrow CO}$	(Kuhlmann et al., 2003)
$j_{CH_3CHOHOOH}$	$CH_3CHOHOOH + h\nu \longrightarrow CH_3 + HCOOH + OH$	j_{CH_3OOH}	(R. Sander et al., 2014)
$j_{Hyetho2h}$	$Hyetho2h + h\nu \longrightarrow HO_2 + CO + OH + CO_2$	$j_{CH_3OOH} + j_{HOCH_2CHO \rightarrow HCO} + j_{HOCH_2CHO \rightarrow CO} + j_{HOCH_2CHO \rightarrow OH}$	(R. Sander et al., 2014)
j_{HCOCO_3H}	$HCOCO_3H + h\nu \longrightarrow HO_2 + CO + OH + CO2$	$j_{Hyetho2h}$	(R. Sander et al., 2014)
j_{HOOCH_2CHO}	$HOOCH_2CHO + h\nu \longrightarrow HCHO + OH + HO2 + CO$	$j_{Hyetho2h}$	(R. Sander et al., 2014)

Acknowledgments

We gratefully acknowledge Stephen Lewis for providing the 1-D atmospheric chemistry sub-module of the LMD-UK MGCM. We also thank Manish Patel for providing insights into Trace Gas Orbiter instruments, and thank Rolf Sander for maintaining the CAABA/MECCA Box model, published under the GNU GPL, which we have used to develop our description of Mars' photochemistry. We thank Sasha Madronich and the National Center for Atmospheric Research for providing the source code of the Tropospheric and Ultraviolet Radiation model used to construct the offline look-up table of photolysis rates of organic compounds that the 1-D model interpolates from. B.M.T. acknowledges his PhD studentship funding (ST/1/R001324/1) from the UK Space Agency, administered by the Science and Technology Facilities Council, as part of the Aurora science programme.

Data archival for this research has begun. The 1-D photochemistry model used to construct the output files analysed and presented in this work is currently stored on the GitHub repository. The offline J-value look-up tables (jmars.20111014 and jmars_organics.nc) are too large to store alongside the 1-D model on GitHub, and will be made available via the University of Edinburgh's Datashare repository. The 1-D model output files themselves used in this research will similarly be stored within the Datashare repository. The TUV model source code used to construct the J-value look-up tables can be acquired through the url https://www2.acom.ucar.edu/modeling/tropospheric-ultraviolet-and-visible-tuv-radiation-model . The Mars Climate Database v5.3 source code used to create the offline tables for atmospheric parameter and long-lived tracer vmr's for the 1-D model here can be acquired through the url http://www-mars.lmd.jussieu.fr/mars/access.html , requiring a request to be made to the researchers listed on the site.

References

Atkinson, R., Baulch, D. L., Cox, R. A., Crowley, J. N., Hampson, R. F., Hynes, R. G., ... Subcommittee, I. (2006). Evaluated kinetic and photochemical data for atmospheric chemistry: Volume ii; gas phase reactions of organic species. *Atmospheric Chemistry and Physics*, *6*(11), 3625–4055. Retrieved from `https://www.atmos-chem-phys.net/6/3625/2006/` doi: 10.5194/acp-6-3625-2006

Baulch, D. L., Bowman, C. T., Cobos, C. J., Cox, R. A., Just, T., Kerr, J. A., ... Warnatz, J. (2005). Evaluated kinetic data for combustion modeling: Supplement ii. *Journal of Physical and Chemical Reference Data*, *34*(3), 757-1397. doi: 10.1063/1.1748524

Baulch, D. L., Cobos, C. J., Cox, R. A., Esser, C., Frank, P., Just, T., ... Warnatz, J. (1992). Evaluated kinetic data for combustion modelling. *Journal of Physical and Chemical Reference Data*, *21*(3), 411-734. Retrieved from `https://doi.org/10.1063/1.555908` doi: 10.1063/1.555908

Campbell, I., & Gray, C. (1973). Rate constants for o(3p) recombination and association with n(4s). *Chemical Physics Letters*, *18*(4), 607 - 609. doi: https://doi.org/10.1016/0009-2614(73)80479-8

Christensen, L. E., Okumura, M., Sander, S. P., Salawitch, R. J., Toon, G. C., Sen, B., ... Jucks, K. W. (2002). Kinetics of ho2 + ho2 h2o2 + o2: Implications for stratospheric h2o2. *Geophysical Research Letters*, *29*(9), 13-1-13-4. doi: 10.1029/2001GL014525

Cody, R. J., Romani, P. N., Nesbitt, F. L., Iannone, M. A., Tardy, D. C., & Stief, L. J. (2003). Rate constant for the reaction ch3 + ch3 c2h6 at t = 155 k and model calculation of the ch3 abundance in the atmospheres of saturn and neptune. *Journal of Geophysical Research: Planets*, *108*(E11). Retrieved from `https://agupubs.onlinelibrary.wiley.com/doi/abs/10.1029/2002JE002037` doi: 10.1029/2002JE002037

Cohen, N., & Westberg, K. R. (1991). Chemical kinetic data sheets for hightem-

perature reactions. part ii. *Journal of Physical and Chemical Reference Data*, *20*(6), 1211-1311. Retrieved from https://doi.org/10.1063/1.555901 doi: 10.1063/1.555901

Dobis, O., & Benson, S. W. (1991). Temperature coefficients of the rates of chlorine atom reactions with c2h6, c2h5, and c2h4. the rates of disproportionation and recombination of ethyl radicals. *Journal of the American Chemical Society*, *113*(17), 6377-6386. Retrieved from https://doi.org/10.1021/ja00017a004 doi: 10.1021/ja00017a004

Fedorova, A., Korablev, O., Bertaux, J.-L., Rodin, A., Kiselev, A., & Perrier, S. (2006). Mars water vapor abundance from spicam ir spectrometer: Seasonal and geographic distributions. *Journal of Geophysical Research: Planets*, *111*(E9). Retrieved from https://agupubs.onlinelibrary.wiley.com/doi/abs/10.1029/2006JE002695 doi: 10.1029/2006JE002695

Fonti, S., & Marzo, G. A. (2010, Mar). Mapping the methane on Mars. *Astronomy and Astrophysics*, *512*, A51. doi: 10.1051/0004-6361/200913178

Forget, F., Hourdin, F., Fournier, R., Hourdin, C., Talagrand, O., Collins, M., ... Huot, J.-P. (1999, October). Improved general circulation models of the Martian atmosphere from the surface to above 80 km. *Journal of Geophysics Research*, *104*, 24155-24176. doi: 10.1029/1999JE001025

Forget, F., Hourdin, F., & Talagrand, O. (1998, February). CO $_2$Snowfall on Mars: Simulation with a General Circulation Model. *Icarus*, *131*, 302-316. doi: 10.1006/icar.1997.5874

Formisano, V., Angrilli, F., Arnold, G., Atreya, S., Bianchini, G., Biondi, D., ... Zasova, L. (2005). The planetary fourier spectrometer (pfs) onboard the european mars express mission. *Planetary and Space Science*, *53*(10), 963 - 974. Retrieved from http://www.sciencedirect.com/science/article/pii/S0032063305000644 (First Results of the Planetary Fourier Spectrometer aboard the the Mars Express Mission) doi: https://doi.org/10.1016/j.pss.2004.12.006

Formisano, V., Atreya, S., Encrenaz, T., Ignatiev, N., & Giuranna, M. (2004). Detection of methane in the atmosphere of mars. *Science*, *306*(5702), 1758–1761. Retrieved from http://science.sciencemag.org/content/306/5702/1758 doi: 10.1126/science.1101732

Friedrichs, G., Herbon, J. T., Davidson, D. F., & Hanson, R. K. (2002). Quantitative detection of hco behind shock waves: The thermal decomposition of hco. *Phys. Chem. Chem. Phys.*, *4*, 5778-5788. Retrieved from http://dx.doi.org/10.1039/B205692E doi: 10.1039/B205692E

Geminale, A., Formisano, V., & Giuranna, M. (2008). Methane in martian atmosphere: Average spatial, diurnal, and seasonal behaviour. *Planetary and Space Science*, *56*(9), 1194 - 1203. Retrieved from http://www.sciencedirect.com/science/article/pii/S0032063308000743 doi: https://doi.org/10.1016/j.pss.2008.03.004

Geminale, A., Formisano, V., & Sindoni, G. (2011). Mapping methane in martian atmosphere with pfs-mex data. *Planetary and Space Science*, *59*(2), 137 - 148. Retrieved from http://www.sciencedirect.com/science/article/pii/S0032063310002138 (Methane on Mars: Current Observations, Interpretation and Future Plans) doi: https://doi.org/10.1016/j.pss.2010.07.011

Giuranna, M., Viscardy, S., Daerden, F., Neary, L., Etiope, G., Oehler, D., ... Amoroso, M. (2019). Independent confirmation of a methane spike on mars and a source region east of gale crater. *Nature Geoscience*. Retrieved from https://doi.org/10.1038/s41561-019-0331-9 doi: 10.1038/s41561-019-0331-9

Gordon, I., Rothman, L., Hill, C., Kochanov, R., Tan, Y., Bernath, P., ... Zak, E. (2017). The hitran2016 molecular spectroscopic database. *Journal of Quantitative Spectroscopy and Radiative Transfer*, *203*, 3 - 69. Retrieved from

http://www.sciencedirect.com/science/article/pii/S0022407317301073 (HITRAN2016 Special Issue) doi: https://doi.org/10.1016/j.jqsrt.2017.06.038

Groß, C. B. M., Dillon, T. J., Schuster, G., Lelieveld, J., & Crowley, J. N. (2014). Direct kinetic study of oh and o3 formation in the reaction of ch3c(o)o2 with ho2. *The Journal of Physical Chemistry A*, *118*(6), 974-985. Retrieved from https://doi.org/10.1021/jp412380z (PMID: 24491030) doi: 10.1021/jp412380z

Guenther, A., Geron, C., Pierce, T., Lamb, B., Harley, P., & Fall, R. (2000). Natural emissions of non-methane volatile organic compounds, carbon monoxide, and oxides of nitrogen from north america. *Atmospheric Environment*, *34*(12), 2205 - 2230. Retrieved from http://www.sciencedirect.com/science/article/pii/S1352231099004653 doi: https://doi.org/10.1016/S1352-2310(99)00465-3

Herron, J. T. (1988). Evaluated chemical kinetic data for the reactions of atomic oxygen o(3p) with saturated organic compounds in the gas phase. *Journal of Physical and Chemical Reference Data*, *17*(3), 967-1026. Retrieved from https://doi.org/10.1063/1.555810 doi: 10.1063/1.555810

Horita, J., & Berndt, M. E. (1999). Abiogenic methane formation and isotopic fractionation under hydrothermal conditions. *Science*, *285*(5430), 1055–1057. Retrieved from https://science.sciencemag.org/content/285/5430/1055 doi: 10.1126/science.285.5430.1055

Joshi, A. V., & Wang, H. (2006). Master equation modeling of wide range temperature and pressure dependence of co + oh products. *International Journal of Chemical Kinetics*, *38*(1), 57-73. doi: 10.1002/kin.20137

Kaufman, F., & Kelso, J. R. (1967). M effect in the gasphase recombination of o with o2. *The Journal of Chemical Physics*, *46*(11), 4541-4543. Retrieved from https://doi.org/10.1063/1.1840589 doi: 10.1063/1.1840589

Korablev, O., Montmessin, F., Trokhimovskiy, A., Fedorova, A. A., Shakun, A. V., Grigoriev, A. V., ... Zorzano, M. P. (2017, Nov 30). The atmospheric chemistry suite (acs) of three spectrometers for the exomars 2016 trace gas orbiter. *Space Science Reviews*, *214*(1), 7. Retrieved from https://doi.org/10.1007/s11214-017-0437-6 doi: 10.1007/s11214-017-0437-6

Korablev, O., Vandaele, A. C., Montmessin, F., Fedorova, A. A., Trokhimovskiy, A., Forget, F., ... Zorzano, M. P. (2019, Apr). No detection of methane on Mars from early ExoMars Trace Gas Orbiter observations. *Nature*, *568*(7753), 517-520. doi: 10.1038/s41586-019-1096-4

Krasnopolsky, V., Bjoraker, G., Mumma, M., & Jennings, D. (1997). High-resolution spectroscopy of mars at 3.7 and 8 m: A sensitive search for h2o2, h2co, hcl, and ch4, and detection of hdo. *Journal of Geophysical Research E: Planets*, *102*(E3), 6525-6534. Retrieved from https://www.scopus.com/inward/record.uri?eid=2-s2.0-17044428646&doi=10.1029%2f96JE03766&partnerID=40&md5=4e1eeef318f69e58131c27b14599b572 (cited By 118) doi: 10.1029/96JE03766

Krasnopolsky, V. A. (2006). Some problems related to the origin of methane on mars. *Icarus*, *180*(2), 359 - 367. Retrieved from http://www.sciencedirect.com/science/article/pii/S0019103505004161 doi: https://doi.org/10.1016/j.icarus.2005.10.015

Krasnopolsky, V. A. (2007). Long-term spectroscopic observations of mars using irtf/cshell: Mapping of o2 dayglow, co, and search for ch4. *Icarus*, *190*(1), 93 - 102. Retrieved from http://www.sciencedirect.com/science/article/pii/S0019103507001005 doi: https://doi.org/10.1016/j.icarus.2007.02.014

Krasnopolsky, V. A. (2011, October). A Sensitive Search for Methane and Ethane on Mars. In *Epsc-dps joint meeting 2011* (p. 49).

Krasnopolsky, V. A. (2012). Search for methane and upper limits to ethane and so2 on mars. *Icarus*, *217*(1), 144 - 152. Retrieved from http://

www.sciencedirect.com/science/article/pii/S001910351100412X doi: https://doi.org/10.1016/j.icarus.2011.10.019

Krasnopolsky, V. A., Maillard, J. P., & Owen, T. C. (2004). Detection of methane in the martian atmosphere: evidence for life? *Icarus*, *172*(2), 537 - 547. Retrieved from http://www.sciencedirect.com/science/article/pii/S0019103504002222 doi: https://doi.org/10.1016/j.icarus.2004.07.004

Kuhlmann, R., Lawrence, M., Crutzen, P., & Rasch, P. (2003, 05). A model for studies of tropospheric ozone and nonmethane hydrocarbons: Model description and ozone results. *Journal of Geophysical Research, v.108 (2003)*, *108*. doi: 10.1029/2002JD002893

Lefèvre, F., & Forget, F. (2009). Observed variations of methane on mars unexplained by known atmospheric chemistry and physics. *Nature*, *460*, 720. doi: 10.1038/nature08228

Lefèvre, F., Lebonnois, S., Montmessin, F., & Forget, F. (2004). Three-dimensional modeling of ozone on mars. *Journal of Geophysical Research: Planets*, *109*(E7). Retrieved from https://agupubs.onlinelibrary.wiley.com/doi/abs/10.1029/2004JE002268 doi: 10.1029/2004JE002268

Lewis, S. R., Collins, M., Read, P. L., Forget, F., Hourdin, F., Fournier, R., ... Huot, J.-P. (1999). A climate database for mars. *Journal of Geophysical Research: Planets*, *104*(E10), 24177-24194. Retrieved from https://agupubs.onlinelibrary.wiley.com/doi/abs/10.1029/1999JE001024 doi: 10.1029/1999JE001024

Madeleine, J.-B., Forget, F., Millour, E., Montabone, L., & Wolff, M. J. (2011, November). Revisiting the radiative impact of dust on Mars using the LMD Global Climate Model. *Journal of Geophysical Research (Planets)*, *116*, E11010. doi: 10.1029/2011JE003855

Madronich, S., Flocke, S., Zeng, J., Petropavlovskikh, I., & Lee-Taylor, J. (2002). Tropospheric ultraviolet and visible (tuv) radiation model. *National Center for Atmospheric Research (NCAR), Boulder, CO. Home page at: http://www. acd. ucar. edu/TUV*.

Mellor, G. L., & Yamada, T. (1982, November). Development of a turbulence closure model for geophysical fluid problems. *Reviews of Geophysics and Space Physics*, *20*, 851-875. doi: 10.1029/RG020i004p00851

Millour, E., Forget, F., Spiga, A., Vals, M., Zakharov, V., Navarro, T., ... MCD/GCM Development Team (2017, April). The Mars Climate Database (MCD version 5.3). In *Egu general assembly conference abstracts* (Vol. 19, p. 12247).

Montabone, L., Forget, F., Millour, E., Wilson, R., Lewis, S., Cantor, B., ... Wolff, M. (2015). Eight-year climatology of dust optical depth on mars. *Icarus*, *251*, 65 - 95. Retrieved from http://www.sciencedirect.com/science/article/pii/S0019103515000044 (Dynamic Mars) doi: https://doi.org/10.1016/j.icarus.2014.12.034

Moores, J. E., King, P. L., Smith, C. L., Martinez, G. M., Newman, C. E., Guzewich, S. D., ... Schuerger, A. C. (2019). The methane diurnal variation and microseepage flux at gale crater, mars as constrained by the exomars trace gas orbiter and curiosity observations. *Geophysical Research Letters*, *46*(16), 9430-9438. Retrieved from https://agupubs.onlinelibrary.wiley.com/doi/abs/10.1029/2019GL083800 doi: 10.1029/2019GL083800

Mulenko, S. (1987). The application of an intracavity laser spectroscopy method for elementary processes study in gas-phase reactions. *Revue Roumaine de Physique*.

Mulenko, S. A. (1980). Investigation of the recombination of the hco radical in an atmosphere of argon and helium by the method of internal resonator laser spectroscopy. *Journal of Applied Spectroscopy*, *33*, 688-694.

Mumma, M. J., Villanueva, G. L., Novak, R. E., Hewagama, T., Bonev, B. P.,

DiSanti, M. A., ... Smith, M. D. (2009). Strong release of methane on mars in northern summer 2003. *Science*, *323*(5917), 1041–1045. Retrieved from http://science.sciencemag.org/content/323/5917/1041 doi: 10.1126/science.1165243

Nair, H., Allen, M., Anbar, A. D., Yung, Y. L., & Clancy, R. T. (1994). A photochemical model of the martian atmosphere. *Icarus*, *111*(1), 124 - 150. Retrieved from http://www.sciencedirect.com/science/article/pii/S0019103584711377 doi: https://doi.org/10.1006/icar.1994.1137

Navarro, T., Madeleine, J.-B., Forget, F., Spiga, A., Millour, E., Montmessin, F., & Määttänen, A. (2014, July). Global climate modeling of the Martian water cycle with improved microphysics and radiatively active water ice clouds. *Journal of Geophysical Research (Planets)*, *119*, 1479-1495. doi: 10.1002/2013JE004550

Orlando, J. J., & Tyndall, G. S. (2001). The atmospheric chemistry of the hc(o)co radical. *International Journal of Chemical Kinetics*, *33*(3), 149-156. Retrieved from https://onlinelibrary.wiley.com/doi/abs/10.1002/1097-4601%28200103%2933%3A3%3C149%3A%3AAID-KIN1008%3E3.0.CO%3B2-1 doi: 10.1002/1097-4601(200103)33:3⟨149::AID-KIN1008⟩3.0.CO;2-1

Pratt, G. L., & Wood, S. W. (1984). Kinetics of the reaction of methyl radicals with oxygen. *J. Chem. Soc., Faraday Trans. 1*, *80*, 3419-3427. Retrieved from http://dx.doi.org/10.1039/F19848003419 doi: 10.1039/F19848003419

Robert, S., Vandaele, A., Thomas, I., Willame, Y., Daerden, F., Delanoye, S., ... Bellucci, G. (2016). Expected performances of the nomad/exomars instrument. *Planetary and Space Science*, *124*, 94 - 104. Retrieved from http://www.sciencedirect.com/science/article/pii/S0032063315301203 doi: https://doi.org/10.1016/j.pss.2016.03.003

Rodrigo, R., Garca-lvarez, E., Lpez-Gonzlez, M. J., & Lpez-Moreno, J. J. (1990). A nonsteady one-dimensional theoretical model of mars' neutral atmospheric composition between 30 and 200 km. *Journal of Geophysical Research: Solid Earth*, *95*(B9), 14795-14810. Retrieved from https://agupubs.onlinelibrary.wiley.com/doi/abs/10.1029/JB095iB09p14795 doi: 10.1029/JB095iB09p14795

Rosner, B. M., & Schink, B. (1995, 11). Purification and characterization of acetylene hydratase of pelobacter acetylenicus, a tungsten iron-sulfur protein. *Journal of bacteriology*, *177*, 5767-72. doi: 10.1128/jb.177.20.5767-5772.1995

Sander, R., Baumgaertner, A., Cabrera-Perez, D., Frank, F., Gromov, S., Grooß, J.-U., ... Tauer, S. (2019). The community atmospheric chemistry box model caaba/mecca-4.0. *Geoscientific Model Development*, *12*(4), 1365–1385. Retrieved from https://www.geosci-model-dev.net/12/1365/2019/ doi: 10.5194/gmd-12-1365-2019

Sander, R., Jckel, P., Kirner, O., Kunert, A., Landgraf, J., Pozzer, A., & Kirner, O. (2014, 11). The photolysis module jval-14, compatible with the messy standard, and the jval preprocessor (jvpp). *Geoscientific Model Development*, *7*, 2653-2662. doi: 10.5194/gmd-7-2653-2014

Sander, S., Abbatt, J., Barker, J., Burkholder, J., Friedl, R., Golden, D., ... Wine, P. (2011, 06). Chemical kinetics and photochemical data for use in atmospheric studies, evaluation no. 17.

Sander, S., Finlayson-Pitts, B., Friedl, R., Golden, D., Huie, R., Keller-Rudek, H., ... Wine, P. (2006, 01). Chemical kinetics and photochemical data for use in atmospheric studies. evaluation no. 15 (jpl publication 06-2).

Sander, S., Friedl, R., Golden, D., Kurylo, M., Huie, R., Orkin, V., ... Finlayson-Pitts, B. (2003, 01). Chemical kinetics and photochemical data for use in atmosheric studies; jpl publication 02-25.

Summers, M. E., Lieb, J. B., Chapman, E., & Yung, Y. L. (2002). Atmospheric biomarkers of subsurface life on mars. *Geophysical Research Letters*, *29*(24),

24-1-24-4. Retrieved from https://agupubs.onlinelibrary.wiley.com/doi/abs/10.1029/2002GL015377 doi: 10.1029/2002GL015377

Taraborrelli, D. (2010). *Isoprene oxidation and its impacts on the atmospheric composition* (Doctoral dissertation, Johannes Gutenberg-Universität, Mainz, Germany). Retrieved from http://d-nb.info/1003538770/34

Tsang, W., & Hampson, R. F. (1986). Chemical kinetic data base for combustion chemistry. part i. methane and related compounds. *Journal of Physical and Chemical Reference Data*, *15*(3), 1087-1279. doi: 10.1063/1.555759

Vago, J., Witasse, O., Svedhem, H., Baglioni, P., Haldemann, A., Gianfiglio, G., ... de Groot, R. (2015, Dec 01). Esa exomars program: The next step in exploring mars. *Solar System Research*, *49*(7), 518–528. Retrieved from https://doi.org/10.1134/S0038094615070199 doi: 10.1134/S0038094615070199

Vandaele, A. C., Korablev, O., Daerden, F., Aoki, S., Thomas, I. R., Altieri, F., ... Zorzano, M. (2019, Apr). Martian dust storm impact on atmospheric H_2O and D/H observed by ExoMars Trace Gas Orbiter. *Nature*, *568*(7753), 521-525. doi: 10.1038/s41586-019-1097-3

Vandaele, A. C., Lopez-Moreno, J.-J., Patel, M. R., Bellucci, G., Daerden, F., Ristic, B., ... the NOMAD Team (2018, Jun 19). Nomad, an integrated suite of three spectrometers for the exomars trace gas mission: Technical description, science objectives and expected performance. *Space Science Reviews*, *214*(5), 80. Retrieved from https://doi.org/10.1007/s11214-018-0517-2 doi: 10.1007/s11214-018-0517-2

Veyret, B., Rayez, J. C., & Lesclaux, R. (1982). Mechanism of the photooxidation of formaldehyde studied by flash photolysis of formaldehyde-oxygen-nitric oxide mixtures. *The Journal of Physical Chemistry*, *86*(17), 3424–3430.

Villanueva, G., Mumma, M., Novak, R., Radeva, Y., Kufl, H., Smette, A., ... Hartogh, P. (2013). A sensitive search for organics (ch4, ch3oh, h2co, c2h6, c2h2, c2h4), hydroperoxyl (ho2), nitrogen compounds (n2o, nh3, hcn) and chlorine species (hcl, ch3cl) on mars using ground-based high-resolution infrared spectroscopy. *Icarus*, *223*(1), 11 - 27. Retrieved from http://www.sciencedirect.com/science/article/pii/S0019103512004599 doi: https://doi.org/10.1016/j.icarus.2012.11.013

Webster, C. R., Mahaffy, P. R., Atreya, S. K., Flesch, G. J., & Farley, K. A. (2013). Low upper limit to methane abundance on mars. *Science*, *342*(6156), 355–357. Retrieved from https://science.sciencemag.org/content/342/6156/355 doi: 10.1126/science.1242902

Webster, C. R., Mahaffy, P. R., Atreya, S. K., Flesch, G. J., Mischna, M. A., Meslin, P. Y., ... Lemmon, M. T. (2015). Mars methane detection and variability at gale crater. *Science*, *347*(6220), 415–417. Retrieved from http://science.sciencemag.org/content/347/6220/415 doi: 10.1126/science.1261713

Webster, C. R., Mahaffy, P. R., Atreya, S. K., Moores, J. E., Flesch, G. J., Malespin, C., ... Vasavada, A. R. (2018). Background levels of methane in mars' atmosphere show strong seasonal variations. *Science*, *360*(6393), 1093–1096. Retrieved from http://science.sciencemag.org/content/360/6393/1093 doi: 10.1126/science.aaq0131

Wong, A. S., & Atreya, S. K. (2004). Atmospheric photochemistry above possible martian hot spots. *Advances in Space Research*, *33*(12), 2236 - 2239. Retrieved from http://www.sciencedirect.com/science/article/pii/S0273117703005246 (Mercury, Mars and Saturn) doi: https://doi.org/10.1016/S0273-1177(03)00524-6

Wong, A.-S., Atreya, S. K., & Encrenaz, T. (2003). Chemical markers of possible hot spots on mars. *Journal of Geophysical Research: Planets*, *108*(E4). Retrieved from https://agupubs.onlinelibrary.wiley.com/doi/abs/10.1029/2002JE002003 doi: 10.1029/2002JE002003

Zahnle, K., Freedman, R. S., & Catling, D. C. (2011). Is there methane on mars? *Icarus*, *212*(2), 493 - 503. Retrieved from `http://www.sciencedirect.com/science/article/pii/S001910351000446X` doi: https://doi.org/10.1016/j.icarus.2010.11.027